

1 **Tectono-stratigraphic evolution of the intermontane Tarom Basin (NW sectors of the**
 2 **Arabia-Eurasia collision zone): insights into the vertical growth of the Iranian Plateau**
 3 **margin**

4
 5 M. Paknia¹, P. Ballato¹, M. Mattei¹, G. Heidarzadeh², F. Cifelli¹, J. Hassanzadeh³, G. Vezzoli⁴,
 6 M. Mirzaie Ataabadi⁵ and M.R. Ghassemi⁶

7
 8
 9 ¹Department of Science, University of Roma Tre, Rome, Italy

10 ²Institute of Earth and Environmental Sciences, University of Potsdam, Potsdam, Germany

11 ³Division of Geological & Planetary Sciences, California Institute of Technology Pasadena,
 12 Pasadena, CA, USA

13 ⁴Department of Earth and Environmental Sciences, University of Milano-Bicocca, Milan, Italy

14 ⁵Department of Geology, Faculty of Science, University of Zanjan, Zanjan, Iran

15 ⁶Research Institute for Earth Sciences, Geological Survey of Iran, Tehran, Iran

16
 17 Corresponding author: Mohammad Paknia (Mohammad.Paknia@uniroma3.it)

18
 19
 20 **Key Points:**

- 21 • In the Tarom Basin arc volcanism terminated at ~38-36 Ma, while intermontane
 22 synorogenic deposition occurred from ~16.5 to < 7.6 Ma
- 23 • The Iranian Plateau formed in the broken retroforeland of the Arabia-Eurasia collision
 24 zone
- 25 • Crustal shortening and thickening cannot be responsible for the vertical growth of the

26 Iranian Plateau margin

27 **Abstract**

28 The intermontane Tarom Basin of NW Iran (Arabia-Eurasia collision zone) is located at the
29 transition between the Iranian Plateau (IP) to the SW and the Alborz Mountains to the NE. This
30 basin was filled by Late Cenozoic synorogenic red beds that retain first-order information on the
31 erosional history of adjacent topography, the vertical growth of the plateau margin and its lateral
32 (orogen perpendicular) expansion. Here, we perform a multidisciplinary study including
33 magnetostratigraphy, sedimentology, geochronology and sandstone petrography on these red
34 beds. Our data show that widespread Eocene arc volcanism in NW Iran terminated at ~ 38-36
35 Ma, while intrabasinal synorogenic sedimentation occurred between ~ 16.5 and < 7.6 Ma,
36 implying that the red beds are stratigraphically equivalent to the Upper Red Formation. After 7.6
37 Ma, the basin experienced intrabasinal deformation, uplift and erosion in association with the
38 establishment of external drainage. Fluvial connectivity with the Caspian Sea, however, was
39 interrupted by at least four episodes of basin aggradation. During endorheic conditions the basin
40 fill did not reach the elevation of the plateau interior and hence the Tarom Basin was never
41 integrated into the plateau realm. Furthermore, our provenance data indicate that the northern
42 margin of the basin experienced a greater magnitude of deformation and exhumation than the
43 southern one (IP margin). This agrees with recent Moho depth estimates, suggesting that crustal
44 shortening and thickening cannot be responsible for the vertical growth of the northern margin of
45 the IP, and hence surface uplift must have been driven by deep-seated processes.

46
47 **KEYWORDS:** Iranian Plateau, plateau margin uplift, deep seated processes,
48 magnetostratigraphy, depositional settings, intermontane sedimentation.

49

50 **1. Introduction**

51 Orogenic plateaus are vast and elevated morphotectonic provinces, which provide the unique
52 opportunity to decipher the interplay between shallow, deep-seated and surface processes, and
53 their influences on Earth's landscape at various timescales (e.g., Dewey et al., 1988; Isacks,
54 1988; Molnar et al., 1993). They contain internally drained basins that have coalesced and have
55 been filled with thick sedimentary deposits and hence retain insights into orogenic, erosional and
56 geodynamic processes (e.g., Alonso et al., 1990; Meyer et al., 1998; Sobel et al., 2003; Strecker
57 et al., 2009; Carrol et al., 2010; Horton et al., 2012; Pingel et al., 2019). Plateau's building
58 models predict that reduced fluvial connectivity promotes basin filling, inhibits intrabasin
59 faulting, and triggers the outward propagation of the deformation fronts. Combined, these
60 processes are thought to be responsible for the lateral (orogen perpendicular) plateau expansion
61 through the integration of new sectors of the foreland into the plateau realm. (Sobel et al., 2003;
62 Garcia Castellanos et al., 2007). The application of these models, however, is not straightforward
63 mostly because the interplay between tectonic and surface processes may trigger different
64 scenarios. This includes basin excavation and erosion with the destruction of the typical plateau
65 morphology (e.g., Strecker et al., 2009; Heidarzadeh et al., 2017). Therefore, while the
66 sedimentary basins in the plateau interior are tectonically stable up to time scales of few 10^7
67 years (e.g., Alonso et al., 1990; Bush et al., 2016), intermontane basins at the transition with the
68 foreland may experience a more complex evolution including several episodes of basin filling
69 and plateau integration, fluvial incision and tectonic deformation at shorter time scales (10^5 to
70 few 10^6 years; e.g., Streit et al., 2015; Schildgen et al., 2016; Tofelde et al., 2017; Ballato et al.,
71 2019; Pingel et al., 2019). Thus, these transitional basins hold precious information on the

72 growth of the plateau margin, the evolution of adjacent mountain ranges, the sediment routing
73 systems and the connectivity history among different sedimentary basins.

74 The NW-SE-oriented Iranian Plateau (IP) is located on the upper plate of the Arabia-Eurasia
75 collision zone and represents the second collisional plateau in elevation and size after Tibet (see
76 Hatzfeld & Molnar, 2010 for a comparison). The IP is parallel to the Zagros orogenic belt and is
77 characterized by high elevation (average elevation is ~1800 m), low internal topographic relief
78 (few hundred of meters), dry climatic conditions, endorheic sedimentary basins in its interior
79 (four out of six basins are internally drained), and steep and dissected flanks bounded by major
80 reverse faults (Ballato et al., 2013, 2017 Heidarzadeh et al., 2017). In central Iran, the northern
81 margin of the IP is marked by a sharp boundary with the adjacent foreland, which comprises the
82 rigid Central Iranian Block (Figure 1). In NW Iran, the IP approaches the Caspian Sea and it is
83 separated from the intracontinental Alborz and Talesh mountains by an elongated, NW-SE
84 oriented intermontane basin called Taron Basin. Currently, this basin is drained by the Qezel-
85 Owzan River, the second largest river in Iran that flows from the interior of the IP to the Caspian
86 Sea. The basin is composed of post Eocene, synorogenic red beds that offer the opportunity to
87 investigate puzzling aspects of this collision zone, such as: the timing and mechanisms of plateau
88 margin uplift, its lateral expansion (i.e., the possible incorporation of the intermontane Taron
89 Basin in the plateau realm) and the link with the adjacent growing Alborz Mountains. For this
90 purpose, we have performed a multidisciplinary study including the characterization of the
91 depositional environments, the sediment provenance areas and the depositional age of the post
92 Eocene synorogenic red beds. Our magnetostratigraphic analysis and new zircon U-Pb ages,
93 document that the widespread Eocene arc volcanism terminated at ~ 38-36 Ma, while the
94 deposition of the red beds occurred from ~16.5 Ma to at least ~7.6 Ma during the growth of the

95 adjacent basin margins. Further, we document the occurrence of alternating periods of efficient
96 and limited fluvial connectivity and we discuss the mechanisms that may have led to the growth
97 of the IP margin in this sector of the Arabia-Eurasia collision zone.
98

99 **1.1. Geological setting**

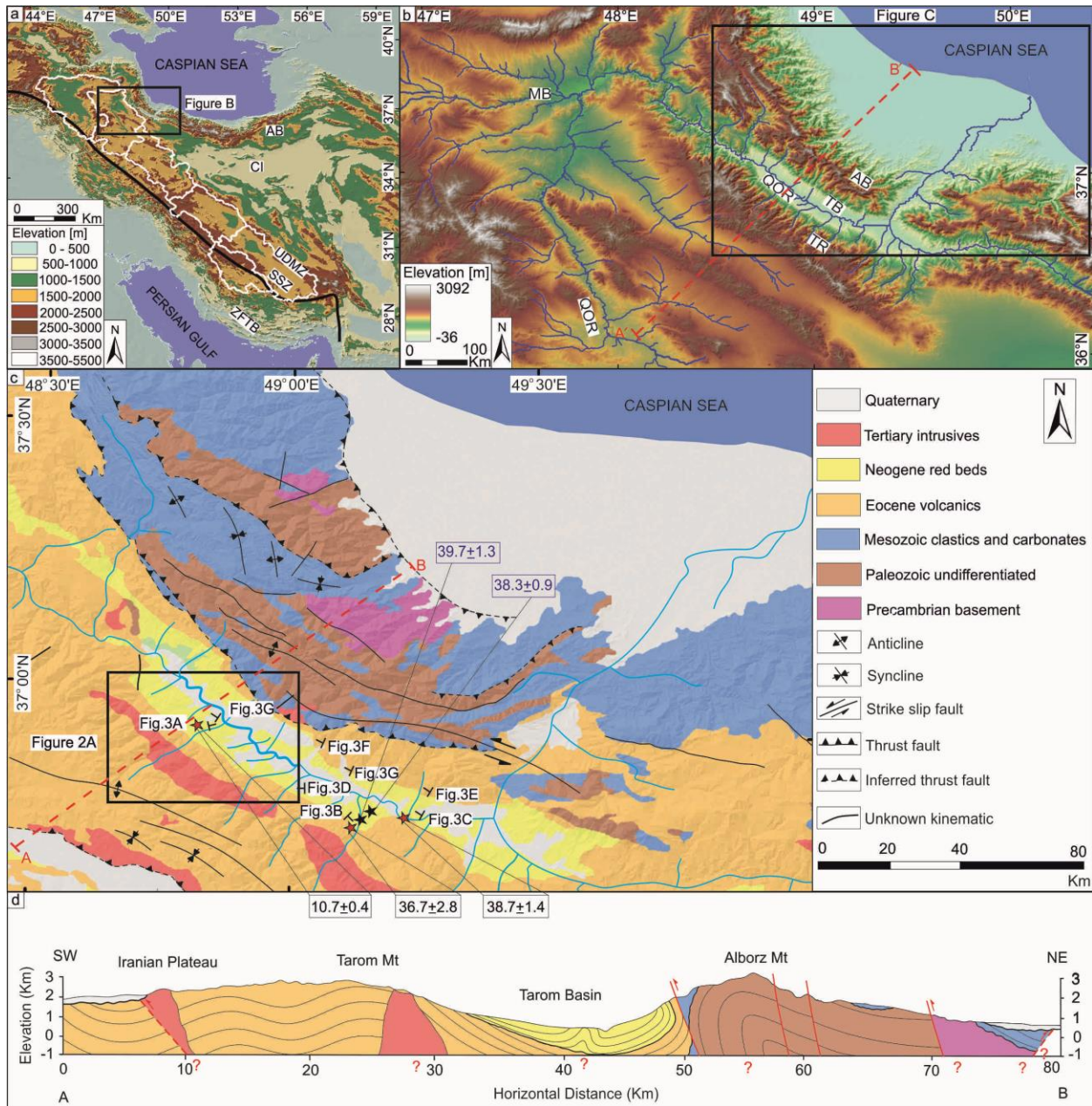
100 The Tarom Basin is a NW-SE oriented, elongated, intermontane basin located along the northern
101 margin of the Iranian Plateau between the western Alborz Mountains to the NE and the Tarom
102 range to the SW (Arabia-Eurasia collision zone; Figure 1).

103 The western Alborz Mountains consist of Pre-Cambrian crystalline basement rocks, Paleozoic
104 and Mesozoic marine deposits, Eocene volcanics, volcanoclastics and intrusives of variable age
105 (Figure 1). This assemblage indicates a complex history of deformation, exhumation,
106 metamorphism, magmatism, subsidence and sedimentation that includes: development of a
107 metamorphic basement during the Neoproterozoic Pan-Africa Orogeny (e.g., Guest et al., 2006;
108 Hassanzadeh et al., 2008), deposition of unconformable carbonate and clastic marine deposits of
109 Pre-Cambrian and Paleozoic age associated with the opening the Paleo-Tethys Ocean (e.g.,
110 Horton et al., 2008), occurrence of the Triassic Cimmerian Orogeny (e.g., Zanchi et al., 2009;
111 Omrani et al., 2013), renewed Mesozoic subsidence with the sedimentation of post-orogenic
112 clastic sediments of the Shemshak Formation (e.g., Zanchi et al., 2009; Wilmesen et al., 2009),
113 deposition of shallow- to deep-marine Middle to Late Jurassic sediments during the opening of
114 the South Caspian Basin (e.g., Brunet et al., 2003), Cretaceous thermal subsidence and marine
115 sedimentation (Brunet et al., 2003), Late Cretaceous to Paleocene deformation and exhumation
116 during a regional compressional event (e.g., Guest et al., 2006; Yassaghi & Madanipour, 2008;
117 Madanipour et al., 2017), deposition of Eocene volcanoclastics in a backarc system associated

118 with the rollback of the Neo-Tethyan oceanic slab (Guest et al., 2006; Ballato et al., 2011, 2013;
119 Verdel et al., 2011; Rezaeian et al., 2012) and finally, contractional deformation and exhumation
120 during the closure of the Neo-Tethys ocean and the collision between Eurasia and Arabia starting
121 from the latest Eocene-earliest Oligocene (e.g., Guest et al., 2006; Ballato et al., 2011, 2013,
122 Rezaeian et al., 2012; Mouthereau et al., 2012; Madanipour et al., 2017, 2018; Pirouz et al.,
123 2017; Koshnaw, et al., 2018). This final event led to development of a narrow, double-verging
124 mountain belt with over 3 km of topographic relief that represents an effective orographic barrier
125 to moist air masses sourced from the Caspian Sea (Figure 1; Ballato et al., 2015). Available low-
126 temperature thermochronology data document slow exhumation from the Early Oligocene
127 followed by an acceleration during the last 12 Ma (Madanipour et al., 2017). Currently, the range
128 accommodates left-lateral shearing between the Caspian Sea and Central Iran (Djamour et al.,
129 2010) and is characterized by the occurrence of few seismogenic faults including the Rudbar
130 Fault, which ruptured in 1990 leading to the catastrophic Mw 7.3 earthquake (Berberian &
131 Walker, 2010). The Taron range consists of a ~ 4-km-thick pile of Eocene volcanic and
132 volcanoclastic rocks of the Karaj Formation (Figures 1 and 2; Stocklin, J., Eftekharneshad, J.,
133 1969) that were deposited in the backarc of the Neo-Tethys subduction zone between ~ 55 and
134 38-36 Ma (Guest et al., 2006; Ballato et al., 2011, 2013; Verdel et al., 2011; Rezaeian et al.,
135 2012). This was associated with the emplacement of Late Eocene (~ 41 to 37 Ma) shallow
136 intrusive rocks (Nabatian et al., 2014). In the Taron range these deposits form a broad, south-
137 verging anticline (Heidarzadeh et al., 2017) with smaller scales anticline-syncline pairs (Figure
138 2), cut by minor high angle (both south and north dipping) reverse faults, locally with a lateral
139 component. Available low-temperature thermochronology data indicate that uplift and

140 exhumation of the Taron range could have started around the latest Eocene-earliest Oligocene
 141 and resumed during the last ~ 10 Ma (Rezaeian et al., 2012).

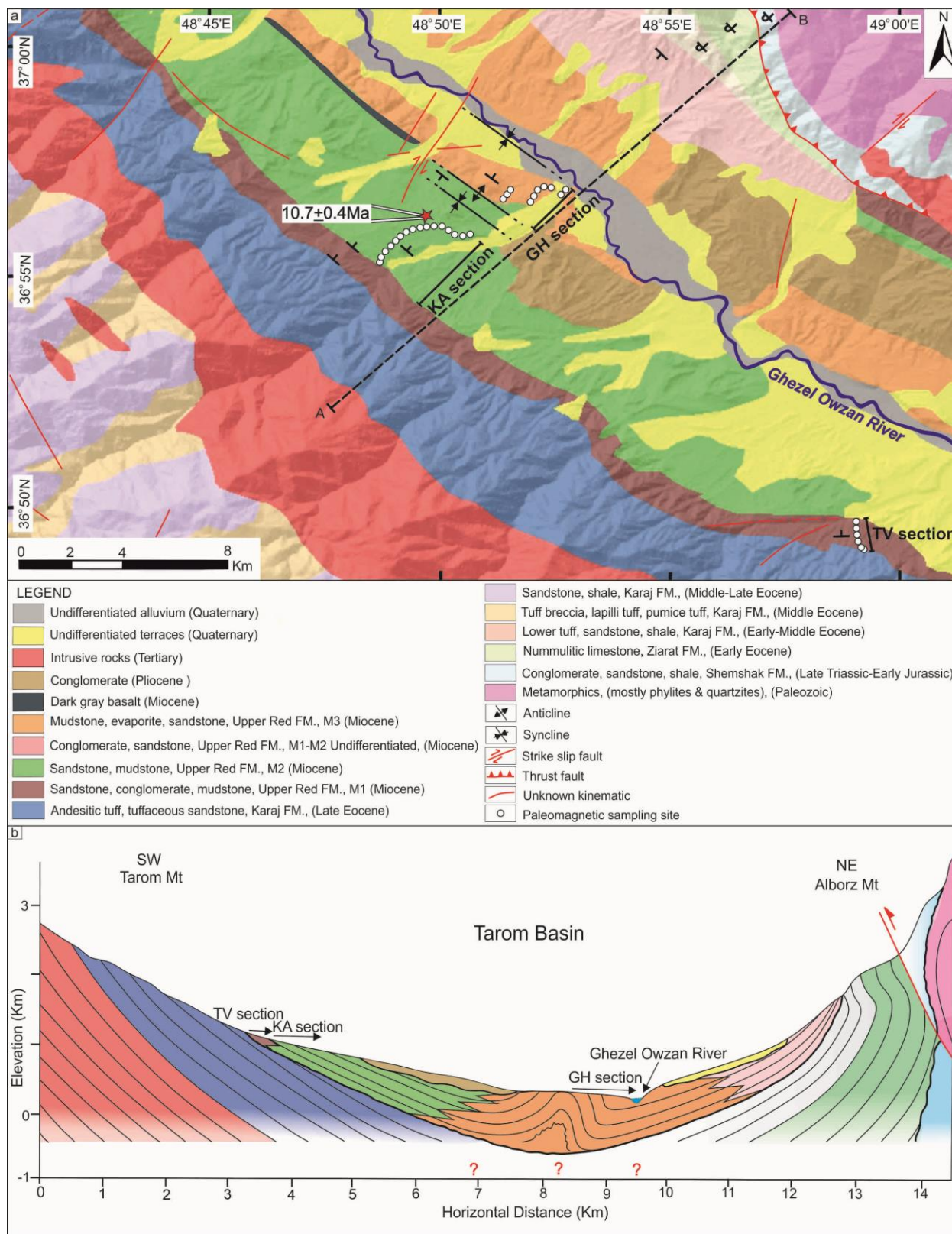
142



143

144 Figure 1. (a) Shuttle Radar Topographic Mission Digital Elevation Model (SRTM DEM) of Iran showing the Iranian
 145 Plateau; the white polygons indicate six main drainage basins forming the Iranian Plateau while the black line shows
 146 the approximate location of the suture zone, which separates the lower Arabian plate (and the Zagros Fold and
 147 Thrust Belt; ZFTB) from the upper Eurasian plate (Ballato et al., 2017). The Urumieh Doktor Magmatic Zone

148 (UDMZ) and the Sanandaj Sirjan Zone (SSZ) represent the backbones and the margins of the plateau, respectively.
149 (b) DEM of NW Iran showing the Mianeh Basin (MB), Tarom Basin (TB) and its bounding Tarom range (TR) and
150 Alborz Mountains (AB), along the southern and the northern margins of the basin, respectively. Note the Qezel-
151 Owzan River (QOR) drainage system ($\sim 55000 \text{ km}^2$) connect the Iranian Plateau and the Caspian Sea through the
152 Tarom Basin. A-A' line shows the approximate location of the crustal scale section shown in figure 14c. (c)
153 Simplified geologic map of NW Iran (Stocklin and Eftekharneshad, 1969; Davies, 1977) showing the location of the
154 panoramic field photographs of figure 3. The red stars show the location of our new zircon U-Pb ages (expressed in
155 Ma); the black stars (and blue ages) represent reworked Eocene volcanic material within red beds that do not
156 provide information on their depositional age. (d) Regional geological cross section (modified after Stocklin et. al,
157 1969).



159 Figure 2. (a) Geologic map (Amini, 1969) superimposed on a SRTM hillshade model of the study area (TB). The
160 white circles show the location of the three sections sampled for magnetostratigraphy named TV, KA and GH. The
161 base of section G is also visible in figure 3h. (b) Geologic cross section across the Tarom Basin.

162

163 **1.3. Regional stratigraphy**

164 The Tarom Basin was filled by post Eocene red beds that rest in angular unconformity onto
165 Eocene volcanics and volcanoclastics of the Karaj Formation (Figure 2). The stratigraphic
166 position of the red beds is unknown, mostly because the Late Oligocene-Early Miocene marine
167 transgression that led to the widespread deposition of the shallow-water marine limestones of the
168 Qom Formation (Reuter et al., 2009) did not reach the Tarom Basin. These marine deposits are
169 sandwiched between the clastic deposits of the Lower Red (LRF; Oligocene) and Upper Red
170 (URF, Miocene) formations and represent a regional marker that can be followed along the
171 southern margin of the Eurasian plate. Therefore, their absence, does not allow differentiating the
172 stratigraphic position of the red beds exposed in the Tarom Basin, which have been considered
173 either Neogene (Stocklin and Eftekharneshad, 1969; Davies, 1977) or Miocene in age (Figures 1
174 and 2; Amini, 1969).

175 The LRF and the URF are exposed virtually everywhere along the southern margin of the
176 Eurasian plate, where they have a thickness varying from few hundreds to few thousands of
177 meters. These red beds are characterized by a variable amount of sandstones, conglomerates,
178 mudstones, evaporites and locally volcanics, and are mostly considered synorogenic sediments
179 associated with collisional deformation (e.g., Morley et al., 2009; Ballato et al., 2008, 2011,
180 2017; Rezaeian, et al., 2012; Madaniopour et al., 2017). Lithologically, the LRF is rather
181 heterogeneous, while the URF seems to have more uniform characteristics, and hence has been
182 differentiated into 3 Units (M1, M2 and M3; e.g., Davoudzadeh et al., 1997). Units M1 and M3

183 are generally dominated by mudstones and evaporites with a variable amount of sandstones and
184 conglomerates while Unit M2 is characterized by abundant sandstones. The URF is superseded
185 by supposed Pliocene conglomerates (Hezadarreh Formation; Rieben et al., 1955) that are
186 generally thought to mark an intensification of collisional deformation (e.g., Rezaeian, et al.,
187 2012; Madaniopour et al., 2017). These conglomerates, however, are diachronous and their age
188 depends on their position with respect to the coeval active mountain fronts. For example, in the
189 southern Alborz Mountains (Ballato et al., 2008) and in the interior of the Iranian plateau (Tavaq
190 Conglomerates, Great Pari Sedimentary Basin; Ballato et al., 2017) conglomeratic deposition
191 started at ~ 7.5 and ~ 10.7 Ma, respectively.

192

193 **1.4. Stratigraphic and structural setting of the Tarom Basin**

194 The red beds of the Tarom Basin consist of coarse- to medium-grained clastic deposits passing
195 laterally toward the basin axis to finer grained sediments and evaporites (Figure 3b). The
196 minimum thickness of the basin-fill sediments observable in the field in the central sectors of the
197 basin is about 1185 m, while the lack of major intrabasinal unconformities within the red beds
198 suggests that sedimentation was rather continuous. In some parts, the red beds are
199 unconformably covered by gently deformed, conglomerates of supposed Pliocene age (Figure
200 3a). Furthermore, at least three generations of terrace conglomerates can be observed in the field,
201 suggesting the occurrence of recent phases of sediment aggradation and fluvial incision (Figure
202 3g).

203 Along the southern margin of the basin, the red beds dip few degrees toward the NE (up to 20°),
204 while the underlying volcanics are generally steeper (Figure 3c) and can be locally folded
205 (Figure 3b). In addition, the southern margin of the basin is characterized by several subvertical

206 synsedimentary normal faults (Figure 3d), mostly parallel to the strike of the basin, that provide
207 evidences for localized extension sub-parallel to the regional shortening direction (NE-SW;
208 Madanipour et al., 2017). These faults are not linked to major extensional events and hence did
209 not control the basin-scale subsidence pattern (Paknia, 2019; PhD thesis; see chapter III).

210 Along the northern side of the basin, the setting is more variable and complex, and the Eocene
211 deposits of the Karaj Formation are either sub-vertical or overturned. In the central-southern
212 sectors of the basin, the unconformable red beds are also subvertical to overturned (Figure 3e)
213 and exhibit a rapid shallowing upward trend suggesting the occurrence of growth strata.
214 Conversely, in the central-northern sectors of the basin the angular unconformity is more
215 pronounced, and the red beds dip less than 30° to the south-west (Figure 3f). There, we do not
216 have evidences for syndepositional contractional deformation.

217 The central sectors of the basin are also characterized by several upright syncline-anticlines
218 pairs, subparallel to the strike of the basin with a lateral extent of few kilometers (Figure 2).
219 Figure 3h shows the core of one of these anticlines which is characterized by evaporites layers
220 that have been deformed in a disharmonic manner and may have acted as local decollement
221 horizon.

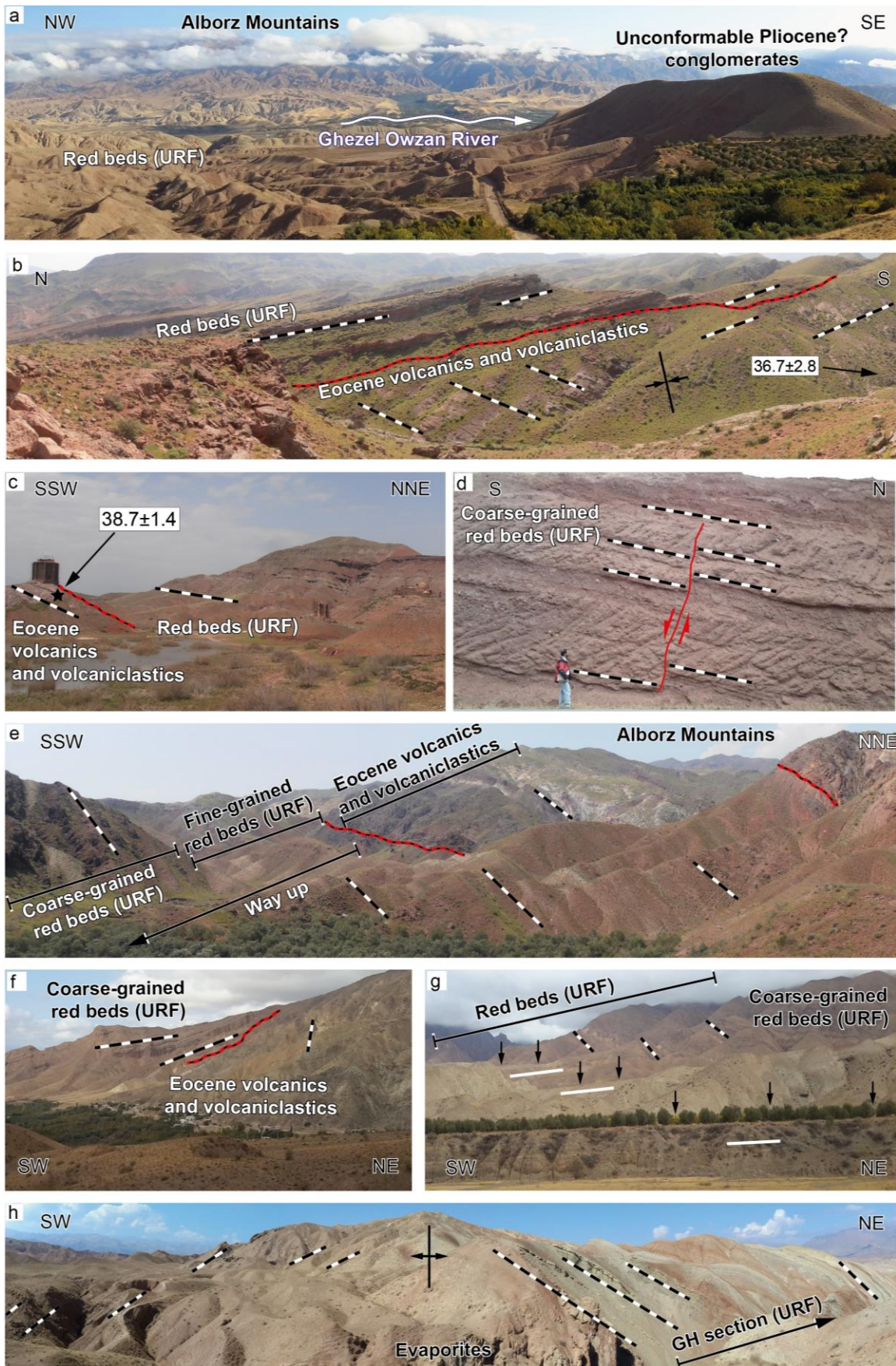
222 Currently, the basin is drained by the ~800 km long Qezel-Owzan River (QOR), which is
223 flowing from the elevated Iranian Plateau to the Caspian Sea (Figure 1). The connection between
224 the interior of the Iranian Plateau, the Taron Basin and the Caspian Sea occurs through a serious
225 narrow bedrock gorges suggesting a protracted history of internal drainage conditions followed
226 by fluvial captures (Heidarzadeh et al., 2017). In particular, the connectivity between the Taron
227 Basin and the Iranian Plateau must have been established during the last 4 Ma through lake

228 overspill as suggested by the stratigraphic record of a sedimentary basin in the plateau interior
229 (Mianeh Basin, Figure 1b; Heidarzadeh et al., 2017).

230

231

232



234 Figure 3. Panoramic field photographs (see figure 1 for location) highlighting the main geometrical relationships
235 among the units and formations exposed in the Tarom Basin. (a) Northeast-facing photo showing conglomerates
236 supposed Pliocene age in unconformity onto deformed red beds; the conglomerates are tilted to the NNE and have a
237 dip angle of ca. 25°. On the foreground the mountain front of the Alborz Mountains with several generation of
238 terraces is visible (see figure g for details). (b and c) Southeast- and northwest-facing photos documenting the
239 unconformity (red and black line) between the Karaj Formation and the red beds in the southern margin of the basin.
240 Black and white dashed lines show the bedding while the zircon U-Pb ages reported are in Ma (see Table 3 and
241 figure 1). (d) Synsedimentary normal fault exposed along the TV sections (Paknia, 2019; PhD thesis; see chapter
242 III). (e and f) Northwest-facing photos documenting the unconformity (red and black line) between the Karaj
243 Formation and the red beds in the southern margin of the basin. Note that in figure e the red beds are overturned. (g)
244 West-facing photo displaying three major terrace conglomerates (see black arrows); these deposits are virtually
245 undeformed (white lines) and cover in unconformity steeply dipping red beds (black and white dashed lines). (h)
246 Northwest-facing photo showing the core of the anticline that represents the base of the stratigraphic section GH.

247

248 **2. Material and methods**

249 To unravel the basin-fill history of the Tarom Basin and its tectono-stratigraphic evolution in the
250 framework of collisional deformation and plateau building processes, we performed a
251 multidisciplinary study including:

- 252 1) A detailed sedimentologic analysis that provides the basis for an assessment of the
253 depositional environments (Tables 1, 2 and 3; see section 3)
- 254 2) A geochronologic study (U-Pb on zircons) of the uppermost volcanic of the Karaj Formation
255 and the red beds that combined with (see section 4)
- 256 3) A paleomagnetic and magnetostratigraphic analyses provides a chronostratigraphic framework
257 for the Late Cenozoic basin-fill sediments (see section 4)

258 4) A provenance study (sandstone petrography and paleocurrent analysis; see section 4), which
259 allows identifying compositional variations related to the exposure of new sediment sources
260 and/or drainage-pattern reorganizations in the sediment source area (Detailed information about
261 the analytical methods are provided in the Appendix section). This approach was employed on
262 two stratigraphic sections exposed along the southern margin of the basin (TV and KA sections;
263 Figure 2) and on a third one located in the northern limb of a north-vergent anticline in the
264 central sectors of the basin (GH section; Figure 2). These sections are stratigraphically
265 continuous and are not affected by major faults, therefore they represent an ideal setting for
266 magnetostratigraphic sampling. Furthermore, recent papers from Central and Northern Iran have
267 shown that the Late Cenozoic red beds have good magnetic properties and hence are suitable for
268 paleomagnetic analysis (Ballato et al., 2008, 2017; Cifelli et al., 2015; Mattei et al., 2015, 2017,
269 2020). The red beds exposed along the southern basin margin (TV and KA section) are tilted
270 northward with a dip angle of 14 to 30°, whereas in the central sectors of the basin (GH section)
271 strata are steeply dipping to the north (and occasionally overturned) with a dip angle of 40 to 88°.
272 The stratigraphic sections along the southern margin cover the lowermost stratigraphic interval
273 of the basin fill and consist mainly of reddish or light brownish conglomerates with intercalations
274 of mudstone and fine-grained sandstone layers evolving up section into channelized sandstones
275 with conglomerate lenses (fluvial channels, see next section) and finer-grained sediments with
276 tabular geometries (flood plain deposits, see next section). The stratigraphic section in the central
277 sectors of the basin consists mainly of reddish, greyish and brownish mudstones, thin bedded
278 sandstones and evaporates layers, locally with intercalations of conglomerates lenses, which
279 become more abundant toward the top of the section.

280

281 **3. Depositional systems in the Tarom Basin**

282 Based on our field observations (lithological characteristics, lateral and vertical grain size
283 variations, sedimentary structures and geometry of the sedimentary bodies) and according to the
284 classification scheme of Miall (1985; 1996), we established a total of eighteen lithofacies types
285 (Table 1 and Figure 4) and recognized eight facies associations (Table 2 and Figure 5). The
286 combination of the facies associations led to the reconstruction of four depositional environments
287 (alluvial fan, braided river, playa-lake and lacustrine settings; Figure 5). In the following, we
288 describe the main characteristics of these depositional settings.

289

290 **3.1. Alluvial fan system**

291 Alluvial fan deposits (Figures 5a and 5b) are located along both margins of the Tarom Basin and
292 include two facies associations: (1) disorganized granule-boulder conglomerate (G1; Figures 4a
293 and 5a), and (2) moderately to well organized granule-boulder conglomerate (G2; Figures 4b and
294 5b). We interpret the G1 facies association with weakly developed clast imbrications and erosive
295 basal contacts as high-energy stream-floods equivalent to those produced by gravel-laden
296 streams or sediment gravity flow deposits (hyperconcentrated and turbulent flow) in poorly
297 confined channels (Figure 4a and 5a; e.g., Maizels, 1989; Stanistreet & McCarthy, 1993;
298 Ridgway & DeCelles, 1993; Miall, 1996; Blair, 1999). The beds geometry suggests the
299 occurrence of sheet flows (Hein, 1982) with limited development of longitudinal bars
300 (Boothroyd & Ashley, 1975; Todd, 1989). The G2 facies association is interpreted as traction-
301 current deposits in poorly confined channels under conditions of higher bed shear stress (Figures
302 4b and 5b; e.g., Stanistreet and McCarthy, 1993; Miall, 1996; Blair, 1999; Ballato et al., 2011).

303

304 **3.2. Braided fluvial system**

305 The braided river deposits (Figures 5c, 5d and 5e) are characterized by four facies associations:
306 (1) well-organized granule-pebble conglomerate (G3), (2) sandstone (S), (3) interbedded fine-
307 grained sandstone and mudstone (SM), and (4) evaporite (E). The G3 facies association is
308 interpreted to reflect traction-current deposits (longitudinal bars or lag deposits) related to the
309 waning stage of high-energy flow in a laterally confined system (e.g., Stanistreet & McCarthy,
310 1993; Miall, 1996; Blair, 1999). The erosive basal contact, together with the lens geometry and
311 the interfingering with stratified sandstones suggests deposition in a braided channel with a
312 variable proportion of gravel and sand (Figures 4c and 5c; e.g., Miall, 1996). The S facies
313 association is interpreted to represent deposition in lower and upper plane-bed flow regimes in a
314 confined flow (e.g., Miall, 1996). Planar (Sp) and trough cross-stratified (St), medium to coarse-
315 grained, pebbly sandstones are interpreted as migrating bedforms (fluvial dunes) in a confined
316 flow in an upper to lower flow regime (Figure 4c; Uba et. al, 2005; Siks & Horton, 2011).
317 Overall, these observations indicate deposition in fluvial channel. The SM facies association
318 (Figure 5d) includes sandstones with cross (Sr; Figure 4d) and planar lamination (Sh and Sl;
319 Figure 5d) that are interpreted as sheet-flow deposits in a poorly confined to unconfined flow
320 evolving from the upper flow regime to a waning flow stage. The SM facies association includes
321 also massive to parallel laminated mudstones (Fm and Fl; Figure 4f), which can be locally
322 dominant and are interpreted to represent suspension fallout deposits (e.g., Ghibaudo, 1992) from
323 standing or slowly moving waters in the floodplain (e.g., Miall, 1977 and 1978). Locally, the SM
324 facies association are characterized by the development of carbonate nodules and rizzolithes
325 indicating paleosols formation (Figure 4g) during lengthy pauses in sedimentation or slow
326 sedimentation rates (e.g., Kraus, 1999). The occasional occurrence of E facies association (Ev;

327 Figure 4h) is interpreted to represent precipitation of salt minerals from concentrated water
328 solution after evaporation of standing water in the floodplain. Complete desiccation of standing
329 water is also documented by mud cracks (e.g., Lowenstein & Hardie, 1985).
330 Finally, in the KA stratigraphic section in proximity of the southwestern basin margin we found,
331 embedded in the fluvial deposits, the BD facies association. This disorganized package of blocks
332 with different size and sediments of variable grain size is interpreted as landslide deposits
333 (sturzstrom) caused by gravitational collapse of the adjacent mountain front (e.g., Hermanns &
334 Strecker 1999; Paknia, 2019; PhD thesis; see chapter III, see also Table 2 this work). This
335 interpretation is further supported by the occurrence of a clay-rich sheared basal contact and the
336 presence of a dense and irregular network of fractures (jigsaw cracks).

337

338 **3.3. Lacustrine system**

339 The lacustrine system is located along the central sectors of the basin (Figures 4e, 4f, 5f and 5f;
340 section GH) and is characterized by two facies associations: (1) mudstone (M) and (2)
341 interbedded fine-grained sandstone and mudstone (SM). Tabular bodies of laminated mudstone
342 of the M facies association are typical of suspension deposits in a lacustrine offshore setting and
343 indicate a deepening of the system (Figure 4f). Lenses of fine grained-sandstone with
344 symmetrical ripple marks interbedded with mudstone (lenticular and waving bedding Figures 4e
345 and 5f) in the SM facies association indicate deposition in the lacustrine shoreface-offshore
346 transition. In few sectors of the GH stratigraphic section, the tabular sandstones with symmetric
347 ripples become dominant suggesting sedimentation in the lacustrine shoreface (e.g., Horton &
348 Schmitt, 1996; Ilgar & Nemeč, 2005; Chakraborty & Sarkar, 2005; Keighley, 2008; Ghinassi et
349 al., 2012). These intervals, however, are relatively rare and generally have a limited thickness (<

350 1 m), therefore most of the lacustrine sediments exposed in the section were deposited either in
351 the offshore or in the shoreface-offshore transition setting.

352

353 **3.4. Playa lake system**

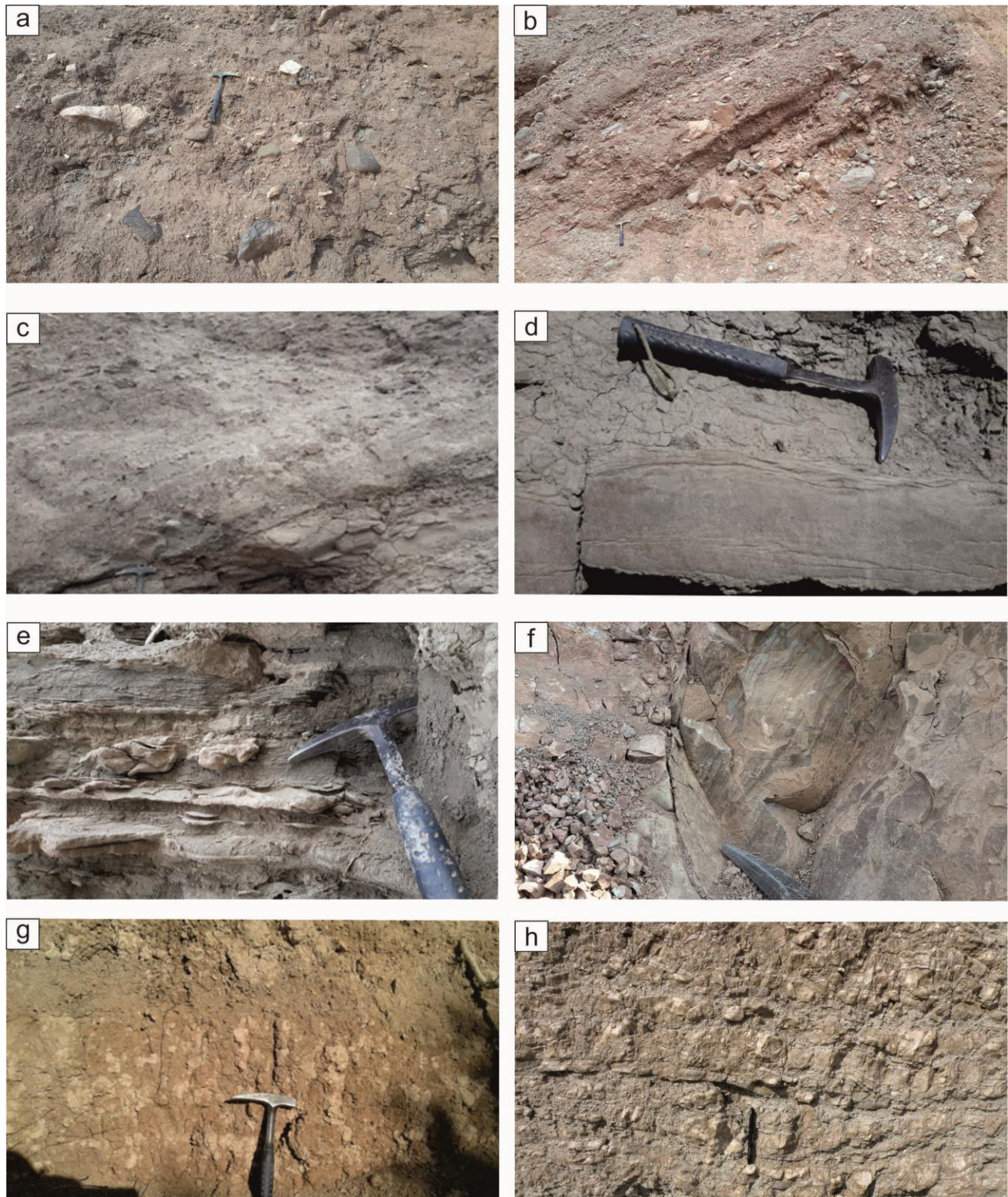
354 The playa lake system is also located in the central sectors of the basin where it alternates with
355 the lacustrine setting (GH stratigraphic section, Figures 4h and 5h). These deposits include two
356 facies associations such as (1) mudstone (M) and (2) evaporite salt minerals (E). The first facies
357 association (mudstone; M) is interpreted to represent deposits settled from suspension in arid to
358 semiarid, oxidizing conditions as documented by the presence of red coloured sediments and the
359 occurrence of desiccation cracks (e.g., Lowenstein & Hardie, 1985). The second facies
360 association (E) is interpreted to represent evaporite layers (mostly gypsum) precipitated during
361 short-lived rain episodes followed by desiccation. Overall, these observations suggest that
362 sedimentation occurred in a shallow playa lake setting.

363

364

365

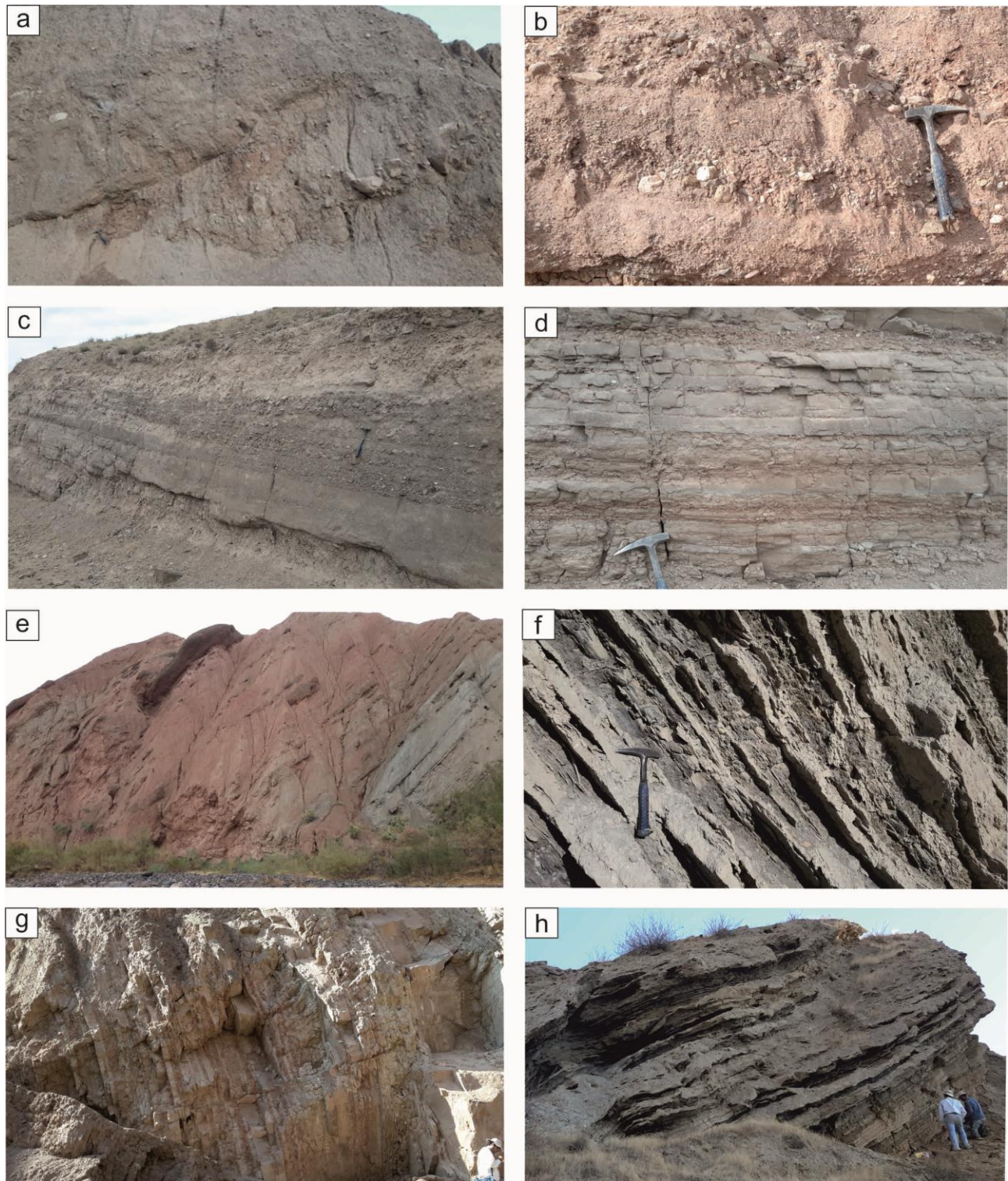
366



367

368 Figure 4. Close up view photographs of lithofacies characteristics. (a) Disorganised, structureless, matrix-supported,
 369 mostly monomictic (clasts are Eocene volcanics) conglomerate with subangular to angular clasts reflecting mass
 370 flow deposits (Facies code Gmd). (b) Disorganised, structureless, clast-supported, mostly monomictic conglomerate

371 with crude bedding and subangular to moderately rounded clasts (stream-flood deposits; Gcd). (c) Conglomerates
372 and coarse-grained sandstones with planar cross bedding representing traction current bedforms (Gp and Sp,
373 respectively). (d) Horizontally laminated sandstone (Sl) and rippled sandstone (Sr) indicating traction currents of
374 variable energy in sandy dominated system. (e) Lenticular bedding with symmetrical rippled sandstone (Smw)
375 alternated with laminated mudstone (Fl) reflecting an alternation of current (bidirectional) and suspension deposits.
376 (f) Massive structureless (Fm) to finely laminated (Fl) calcareous mudstone (suspension deposits). (g) Mudstone
377 with carbonate nodules (P) indicating paleosol formation. (h) Evaporate deposits (Ev) reflecting evaporation from
378 standing water.
379



380

381 Figure 5. Representative views of different depositional systems in the Tarom Basin. (a) Disorganized granule-
 382 boulder conglomerate (facies association G1; base of KA stratigraphic section) and (b) moderately to well organized
 383 granule-boulder conglomerate (facies association G2; KA stratigraphic section) representing an alluvial fan setting.

384 (c) Horizontally to trough cross-stratified pebbly sandstone and conglomerate in a fluvial channel (facies association
 385 S; KA stratigraphic section), of a braided river system. (d) Horizontally, thin bedded, fine grained sandstone and
 386 laminated mudstone sheets (facies associations SM; KA stratigraphic section) representing flood plain deposits of
 387 the braided river system. (e) Overview of the braided river system with lenses of conglomerate and coarse-grained
 388 sandstone (facies association S and G3) embedded in flood plain deposits (facies associations SM; top of GH
 389 stratigraphic section). (f) Fine grained sandstone and mudstone deposits with flat geometry (facies association SM;
 390 GH stratigraphic section) reflecting deposition in the shoreface-offshore transition in a lacustrine depositional
 391 setting; the sandstone layers indicate distal storm beds. (g) Alternation of mudstone and fine-grained sandstone
 392 deposit with flat to tabular geometry (facies association SM; base of GH stratigraphic section; lacustrine
 393 depositional setting); when the mudstone dominates deposition occurred in the offshore setting, otherwise the
 394 alternation of mudstone and sandstone indicates deposition in the shoreface-offshore transition. (h) Gypsum layers
 395 (Evaporite deposits) precipitated during short-lived desiccation episodes (facies association E, GH stratigraphic
 396 section), representing a playa lake depositional setting.

397

398 **Table 1**

399 *Description and Interpretation of Lithofacies*

Facies code	Characteristics	Interpretation
Gmd	Disorganised, structureless, matrix-supported, mostly monomictic conglomerate. Granules to boulders, subangular to angular clasts. Maximum clast diameter 40 cm	Mass flows deposits from hyperconcentrated or turbulent flow
Gcd	Disorganised, structureless, clast-supported, mostly monomictic conglomerate with crude bedding. Granules to boulders, subangular to moderately rounded clasts. Maximum clast diameter 40 cm	Stream-floods deposits with concentrated clasts
Gco	Moderately organized, clast supported, monomictic to polymictic conglomerate. Granules to cobbles, subangular to rounded clasts, normal grading, and weak imbrication. Maximum clast diameter 20 cm	Traction bedload deposits
Gh	Clast-supported, horizontally bedded, monomictic to polymictic conglomerate. Granules to pebbles, subrounded to well-rounded clasts, normal to inverse grading with imbrication. Maximum clast diameter 5 cm	Traction current bedforms (bars)

Gt	Clast-supported, trough cross-stratified, monomictic to polymictic conglomerate. Granules to pebbles, subrounded to well-rounded clasts, normal grading. Maximum clast diameter 5 cm	Traction current bedforms (bars)
Gp	Clast-supported planar cross-stratified monomictic to polymictic conglomerate. Granules to pebbles, subrounded to rounded, normal grading. Maximum clast diameter 5 cm	Traction current bedforms (bars)
Br	Matrix supported, structureless monomictic breccia. Granules to boulders, very angular clasts, inverse grading. Maximum clast diameter 1 m	Rock avalanche deposits (sturzstrom)
Sp	Planer cross-stratified sandstone. Medium to coarse grain size, moderately to well sorted occasionally with pebbles	Dune migration during upper to lower flow regime
Sl	Horizontally laminated sandstone. Very fine to medium grain size, well sorted occasionally with pebbles	Bedforms deposited under upper to lower flow regime
Sr	Rippled sandstone (asymmetric ripples). Very fine to medium grain size, well sorted	Ripples under lower flow regime
Sh	Horizontally stratified sandstone. Very fine to coarse grain size, moderately to well sorted, occasionally with pebbles	Planar bed flow during upper flow regime
St	Trough cross-stratified sandstone. Medium to coarse grain size moderately to well sorted, occasionally with pebbles	Dune migration during upper to lower flow regime
Smw	Rippled sandstone (symmetrical ripples). Fine to medium-grain size well sorted	Wave (bidirectional current) deposits
Fm	Massive structureless calcareous mudstone	Suspension deposits, overbank or abandoned channel
Fl	Finely laminated calcareous mudstone. Flat parallel lamination, small-scale ripples, locally with mud cracks	Suspension deposits, overbank or abandoned channel
Mr	Sheared reddish clay with unsorted angular clasts	Shearing stress at the base of a rock avalanche
P	Mudstone to fine-grained sandstone with carbonate nodules	Paleosol formation
Ev	Evaporites, locally associated with gypsum-filling fractures	In situ accumulation during evaporation of standing water

400

401

402 **Table 2**

403 *Description, Lithofacies, Architectural Elements, and Interpretation of Depositional Processes and Environments of*

404 *Facies Association*

Facies association	Description	Lithofacies	Architectural elements	Interpretation of depositional process	Depositional setting
G1 (disorganized granule-boulder conglomerate)	Structureless to poorly organized, matrix-to clast-supported conglomerate. Beds 0.2 to 1 m thick with lateral extent of few tens of meters and a planar to slightly erosive basal contacts. Interbedded with facies associations G2 and G3	Gmd, Gcd	Gravel sheets and poorly confined channels	Sediment gravity-flow deposits	Alluvial-fan system
G2 (moderately to well organized granule-boulder conglomerate)	Moderately to well-organized, clast-supported, ungraded to normally graded, moderately to poorly sorted, poorly imbricated conglomerate. Moderate to poor horizontal and trough cross-stratification. Beds 0.2- to 1-m-thick with a lateral extent of few tens of meters and a slightly erosive basal contact. Interbedded with facies associations G1, G3, S and SM	Gco, Gh, Gt	Gravel sheets, and gravel downstream accretion macroforms (bars)	Traction bedload deposits in a gravel-dominated, poorly confined channel or in a gravel sheet	Alluvial-fan system
G3 (well organized granule-cobble conglomerate)	Well organized, clast-supported, channelized, horizontally, planar and trough cross-bedded, moderately to well sorted, conglomerate with slightly erosional contacts and a lateral extent of up to tens of meters. Interbedded with facies associations S, G2, SM, and rarely M	Gco, Gp, Gh, Gt, Sh, St, Sp	Channel-fill complex and gravel bedforms (gravel bars and lenses)	Traction bed load deposits in a gravel-dominated, well-confined channel	Alluvial-fan and proximal fluvial system
DB (Disorganized, granules to boulder breccia)	Chaotic, matrix supported, poorly sorted breccia with a sheared clay basal contact and few tens of meters lateral extent	Br, Mr	Probably lobate (full geometry not exposed)	Gravitational collapse from the adjacent mountain front	Landslide deposits (sturzstrom)
S (sandstone)	Channelized, fine to medium-grained, locally coarse-grained to pebbly, normally graded, fining upward sandstone. Sedimentary structures include horizontal, planar and trough cross-bedding and towards the top of the sandstone body ripples and parallel lamination. Beds 0.3-	Sh, St, Sp, Sl, Sr, Gh, Gt, Gp	Channel-fill complex, sandy bedforms and sandy downstream accretionary	Channel fill deposits in a well-confined sand-dominated fluvial channel	Fluvial system (channel complex)

	to 1.5-m-thick with lateral extent of few tens of meters. Erosive concave-up base contacts. Interbedded with facies G3, SM, M, and rarely E		macroforms		
SM (interbedded fine-grained sandstone and mudstone)	<p>Fine-grained sandstone and siltstone with a tabular geometry. Sedimentary structures include parallel lamination symmetrical and asymmetrical ripples locally climbing. Beds 0.1- to 0.5-m-thick, and a lateral extent up to several tens of meters. Basal contacts are flat, non-erosive, and rarely slightly concave up. Proportion between mudstone and sandstone variable. Locally, palaeosol horizons consisting of mottled mudstone and calcite nodules, developed. Interbedded with facies S, G3, M and locally E (in this case they are associated with gypsum-filled fractures)</p>	Sh, Sl, Sr, Smw Fl, Fm, P	Sheet-like and wedging deposits	Sheet-flow deposits in poorly confined to unconfined flow, evolving from upper flow regime to waning flow stage and suspension from standing water, and lacustrine sediments deposited either above the mean fair-weather wave base (sandstone dominating) or above the mean storm wave base (mudstone dominating)	Fluvial (floodplain), playalake and lacustrine system (beach to nearshore and offshore environment)
M (mudstone)	Massive to laminated grey to light red mudstone. Locally, poorly developed calcrete as well as gypcrete. Beds with a flat non-erosive contact typically 0.02- to 0.5-m-thick and a lateral extent up to several tens of meters. Interbedded with facies S, SM, and locally E (in this case they are associated with gypsum-filled fractures)	Fl, Fm, P	Sheet-like	Suspension deposits in standing water	Fluvial (floodplain), playalake and lacustrine system (offshore)
E (evaporite)	Evaporite deposits, 0.05 to 0.3 m thick with a lateral extent of several tens of meters. Generally associated with gypsum-filled fractures. They can form packages of	Ev	Sheet-like	Evaporation deposits from standing water	Playalake or fluvial (highly

	up to 20 m. Interbedded with facies M, rarely with SM and S				evaporativ e flood plain) system
--	--	--	--	--	---

405

406

407 **4. Results**

408 **4.1. Zircon U-Pb geochronology**

409 Five samples were collected for Zircon U-Pb dating in the Eocene volcanics and the Neogene red
 410 clastics to constrain the top age of the Karaj Formation and provide independent age constrains
 411 on the depositional age of the synorogenic red beds. Results are shown in table 3 and in the
 412 Appendix A1.

413 The contact between the Karaj Formation and the overlying red beds is well exposed along both
 414 margins of the basin. Considering that the northern margin has experienced a greater degree of
 415 deformation and erosion (compare Figures 3b and 3c with Figures 3e and 3f) we sampled the
 416 contact along the southern margin of the basin in two different locations (Figure 1). Sample GH-
 417 15-03 represents a > 20-m-thick white tuff that can be followed along strike for about five
 418 kilometers. This lithotype is stratigraphically located below a thick package (several tens of
 419 meters) of coarse-grained volcanoclastic deposits that are less suitable for zircon U-Pb dating and
 420 represent the top of the Karaj Formation in this area (Figure 3b). These units are characterized by
 421 a system of open syncline-anticline pairs with a wavelength of several tens of meters (Figures 3b
 422 and 6). Our tuff sample (GH-15-03) yielded only few zircon grains with a weighted average age
 423 of 36.7 ± 2.6 Ma (Table 3). We collected another sample (GH-15-01) along strike to the SE from
 424 a rhyolite exposed on top the Karaj Formation (Figure 3c). In this area the angular unconformity
 425 with the overlaying red beds has a low angle ($< 10^\circ$). This sample yielded a weighted average

426 age of 38.7 ± 1.4 Ma. This age overlaps with the previous sample (within a two-sigma error)
427 suggesting that the termination of widespread arc volcanism should have occurred sometime
428 between 38 and 36 Ma. This age agrees with those obtained by previous studies (~ 36 Ma,
429 Ballato et al., 2011; ~ 37 Ma, Verdel et al., 2011) in central and northern Iran.

430 An additional, few cm-thick, ash layer (TM-16-01) was collected within the red beds in
431 proximity of the top of the KA stratigraphic section. This sample is fundamental for pinpointing
432 the magnetostratigraphic correlation (see next sections) and yielded a weighted average age over
433 13 grains of 10.7 ± 0.4 Ma (Table 3). This value does not include nine grains that clustered
434 around 13-12 Ma. If we include these grains the weighted average age over 22 grains will be
435 11.3 ± 0.5 Ma (Table 3). Considering that a ~ 10.7 -My-old tuff has been dated about 120 km to
436 the NW in three different locations (Ballato et al., 2017), we prefer to consider the 10.7 Ma
437 option as more reliable than the 11.3 Ma. Accordingly, the 13-12-My-old zircon grains should
438 represent crystals that spent 2-3 million of years in the magmatic chamber before the eruption.

439 Finally, two more samples were collected in the red beds, directly upsection of sample GH-15-
440 03. These two samples are located right above the unconformity (GH-15-02, resampled in a
441 second stage as GH-17-02) and about 400 m (stratigraphically) above it (GH-17-04; Figure 6).
442 The first sample is a weathered, reworked white tuff, while the second one is a light green
443 tuffaceous sandstone with very pristine biotite crystals. These samples gave very similar ages
444 (39.7 ± 1.3 and 38.3 ± 0.9 Ma, respectively; Table 3), which look almost identical to those
445 obtained for the top of the Karaj Formation. Therefore, based on the stratigraphic separation
446 between them we consider these two samples as reworked volcanic material from the eroding
447 Karaj Formation that does not provide indication about the depositional age of the red beds.

448 Combined, our new zircon ages indicate that arc volcanism in this area must have lasted until 38-
 449 36 Ma, while the deposition of the red beds appears to have occurred during the Miocene.

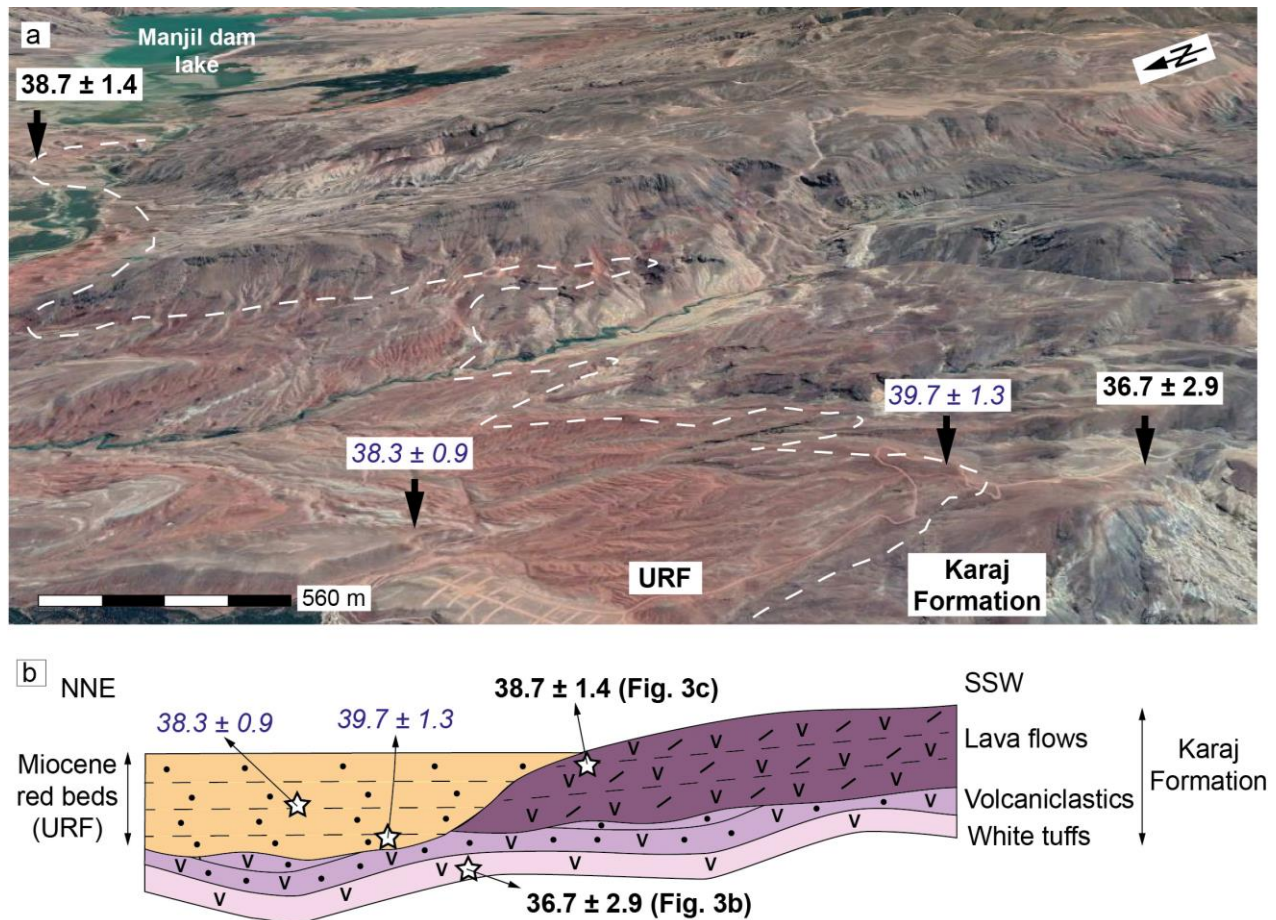
450

451 **Table 3**

452 *Zircon U-Pb Dating Results*

Sample code	Age (Ma)	Error 2s (Ma)	N of grains analyzed	N of grains used	MSWD	Rock type	Formation / Unit	Lat (Dec°)	Long (Dec°)	Elevation (m)
GH-15-01	38.7	1.8	11	10	0.4	Rhyolite	Karaj F	36.74525	49.23086	375
GH-15-02/ GH-17-02	39.7	1.3	18	16	1.8	Reworked tuff	Red Beds	36.70804	49.14391	752
GH-15-03	36.7	2.8	6	4	0.8	White tuff	Karaj F	36.70342	49.14172	840
GH-17-04	38.3	0.9	10	10	1.0	Tuffaceous sandstone	Red Beds	36.72139	49.14806	576
TM-16-01	10.7	0.4	24	13	1.3	Ash	Red Beds	36.91298	48.83748	600
TM-16-01 alternative	11.3	0.5	24	22	3.8					

453



454

455 Figure 6. (a) Google Satellite Imagery showing the relationship between the Karaj Formation and the red beds along
 456 the southern margin of the basin in proximity of the Manjil dam lake (see the same ages reported figure 1 for
 457 location). (b) Schematic cartoon showing the geometrical relationships between the top of the Karaj Formation and
 458 the red beds along the southern margin of the Tarom Basin.

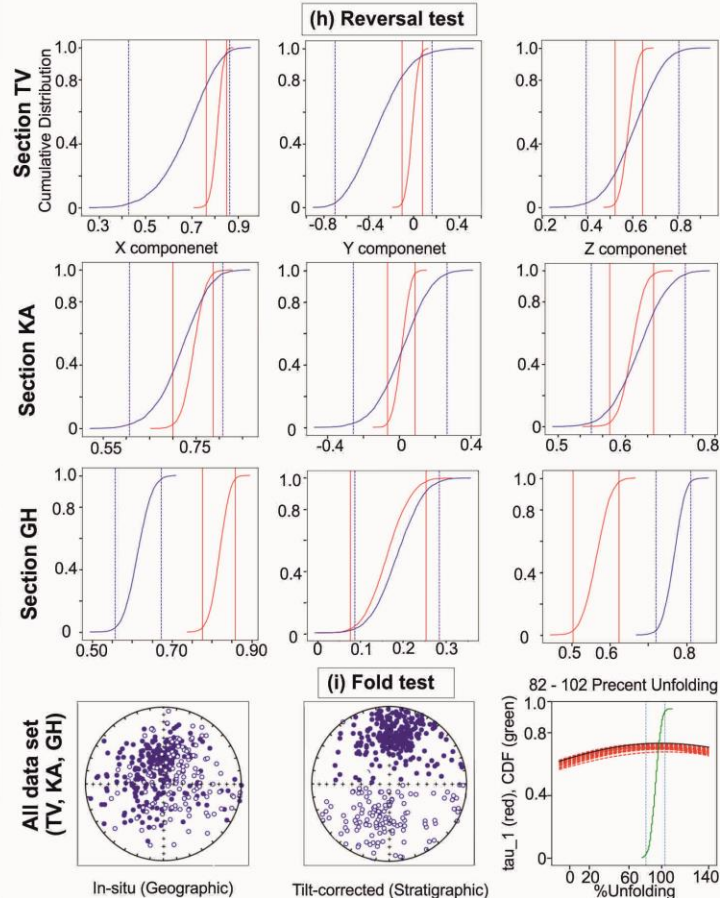
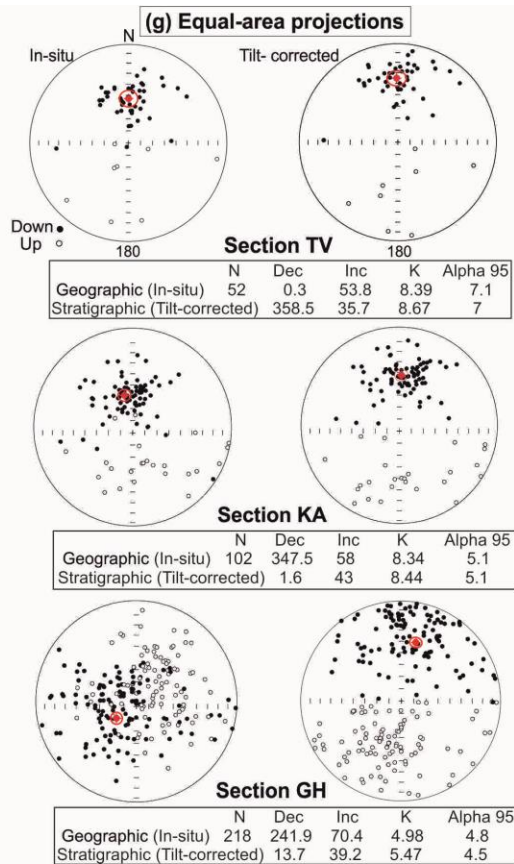
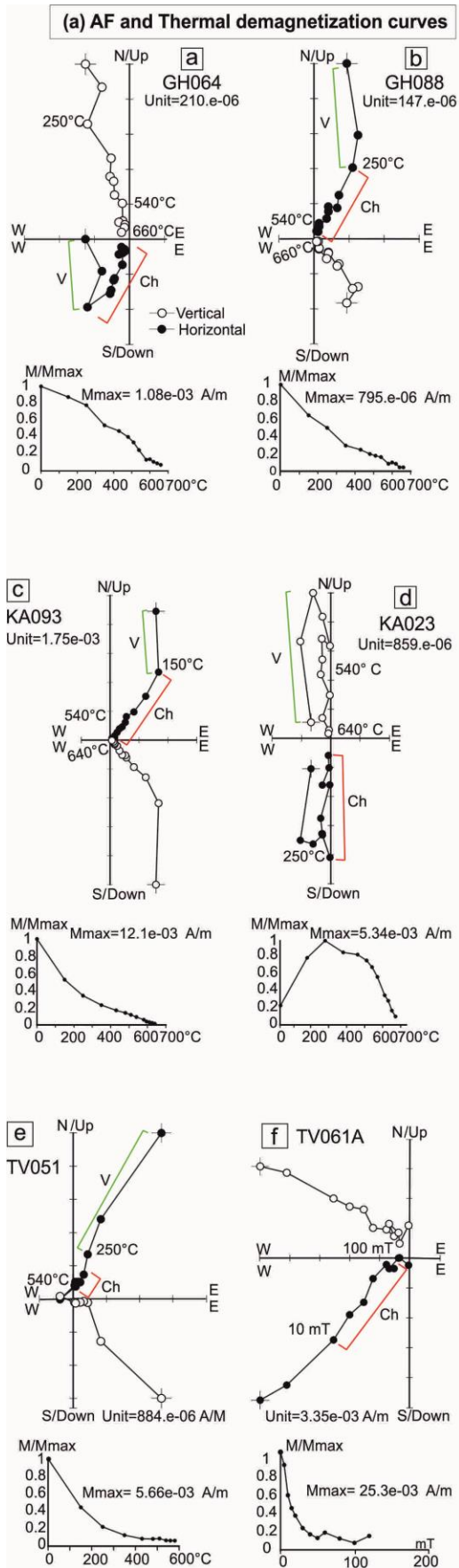
459

460 4.2. Paleomagnetic results

461 Seventy-two samples were collected along the 153-m-thick TV stratigraphic section (M1
 462 member), while 143 and 321 samples were collected from the 565-m-thick KA (M2 member)
 463 and the 1185-m-thick GH Section (M3 member), respectively. Paleomagnetic sampling was
 464 carried out using an ASC 280E petrol-powered transportable drill with a water-cooled diamond
 465 bit. Cores were oriented in situ using a magnetic compass. Five hundred thirty-four samples were

466 measured at the Alpine Laboratory of Paleomagnetism (ALP) at Peveragno (Turin) and at the
467 INGV Laboratory of Paleomagnetism (Rome, Italy) shielded room, using a 2G Enterprises DC-
468 SQUID (superconducting quantum interference device) cryogenic magnetometer. Data were
469 analysed using the software Remasoft 3.0 (Chadima & Hrouda, 2006). The NRM of one
470 specimen per core was measured by means of progressive stepwise demagnetization using
471 thermal (384 specimens) or alternating field (AF) (150 specimens) procedures. Thermal
472 demagnetization was carried out using temperature increments (80-100°C up to 430°C and 30-
473 50°C above 430°C) until the NRM decreased below the limit of instrument sensitivity or random
474 changes appeared in the paleomagnetic directions. Stepwise AF demagnetization was carried out
475 using a set of three orthogonal AF coils mounted in-line with the Superconducting Rock
476 Magnetometers (SRM) system, with 5–10 mT increments up to 20 mT, followed by 20 mT steps
477 up to 120 mT.

478 One hundred sixty-two samples were either too weakly magnetized to allow reliable complete
479 stepwise demagnetization or gave unstable directions during stepwise demagnetization. Such
480 samples were discarded from further analyses. In most of the remaining samples, after the
481 removal of a viscous low temperature/low coercivity normal polarity component at 180°/250° C
482 or 10-30 mT, the NRM vectors aligned along a single linear path toward the origin of the
483 orthogonal diagrams for both normal and reverse polarities (Figure 7a-f). In these samples
484 ChRM directions were calculated by principal component analysis (PCA) (Kirschvink, 1980) of
485 the linear component between 250/320°C and 530/660°C.



487 Figure 7. (a) Tilt corrected diagrams of Thermal and AF demagnetization analysis of representative samples.
488 Demagnetization diagrams and intensity decay curves are shown to the left. The black and white circles represent
489 projections onto the horizontal and vertical plane, respectively (Zijderveld, 1967), while numbers at each
490 demagnetization step denote temperatures in °C (150 to 680) and magnetic field values in mT (5 to 120). (b) Mean
491 normal and reverse polarity of ChRM components for the three investigated stratigraphic sections on equal-area
492 stereographic projection in geographic and tilt-corrected coordinates (Dec = declination; Inc = inclination; K =
493 precision parameter, α_{95} = semi-angle of the cone of 95% confidence). (c) Bootstrap reversal test results for the
494 three stratigraphic sections and (d) fold test results for the entire dataset (Tauxe et al., 1991). The reversal test on TV
495 and KA samples is positive, while GH samples show a negative reversal test. The fold test (all samples from the
496 three studied sections) is positive.

497

498 **4.2.1. TV stratigraphic section**

499 In the TV Section the initial Natural Remnant Magnetization (NRM) intensities vary between
500 8.59×10^{-4} and 1.01×10^{-2} A/M (Figure 8). The highest NRM values (average of 4.34×10^{-2}
501 A/M) were obtained in the alluvial fan deposits at the base of the section (first ~15 m; Figure 8).
502 The bulk susceptibility (k) values range from 170 to 10970×10^{-6} SI (Figure 8). High k values
503 are most probably related to the significant contribution of the volcanoclastic Karaj Formation
504 which is particularly rich in magnetite (Ballato et al., 2008). In the TV Section a reliable ChRM
505 has been obtained in 54 samples, 8 with a reverse polarity and 45 with a normal polarity. The
506 maximum angular deviation (MAD) of the recognized magnetic components is lower than 10°
507 (52 samples) except for two samples where it is 11.2° and 14.9° .

508

509 **4.2.2. KA stratigraphic section**

510 In the KA Section the initial Natural Remnant Magnetization (NRM) intensities vary between
511 9.91×10^{-4} and 1.01×10^{-2} A/M, whereas the bulk susceptibility (k) values range between 460

512 and 26570×10^{-6} SI (Figure 9). As for the TV Section these high values are probably related to
513 the presence of detrital magnetite from the Karaj Fm. In the KA Section a reliable ChRM has
514 been obtained in 102 samples, 25 with a reverse polarity and 77 with a normal polarity. The
515 maximum angular deviation (MAD) of the recognized magnetic components is lower than 10° in
516 85 samples and it varies between 10.2 and 14.8° in 18 samples.

517

518 **4.2.3. GH stratigraphic section**

519 NRM intensities for the GH samples are about one order of magnitude lower than the other two
520 sections, and vary between 9.89×10^{-5} and 1.01×10^{-3} A/M (Figure 10). Magnetic susceptibility
521 (k) values are also lower than those recorded in the other sections, and range from 70 to $3650 \times$
522 10^{-6} SI, possibly reflecting a more composite sediment source area (Figure 10). In the GH
523 Section a reliable ChRM has been obtained in 218 samples, 98 with a reverse polarity and 120
524 with a normal polarity. The maximum angular deviation (MAD) of the recognized magnetic
525 components is lower than $< 10^\circ$ in 200 samples and is comprised between 10.1 and 14.8° in 18
526 samples.

527

528

529

530

531

532

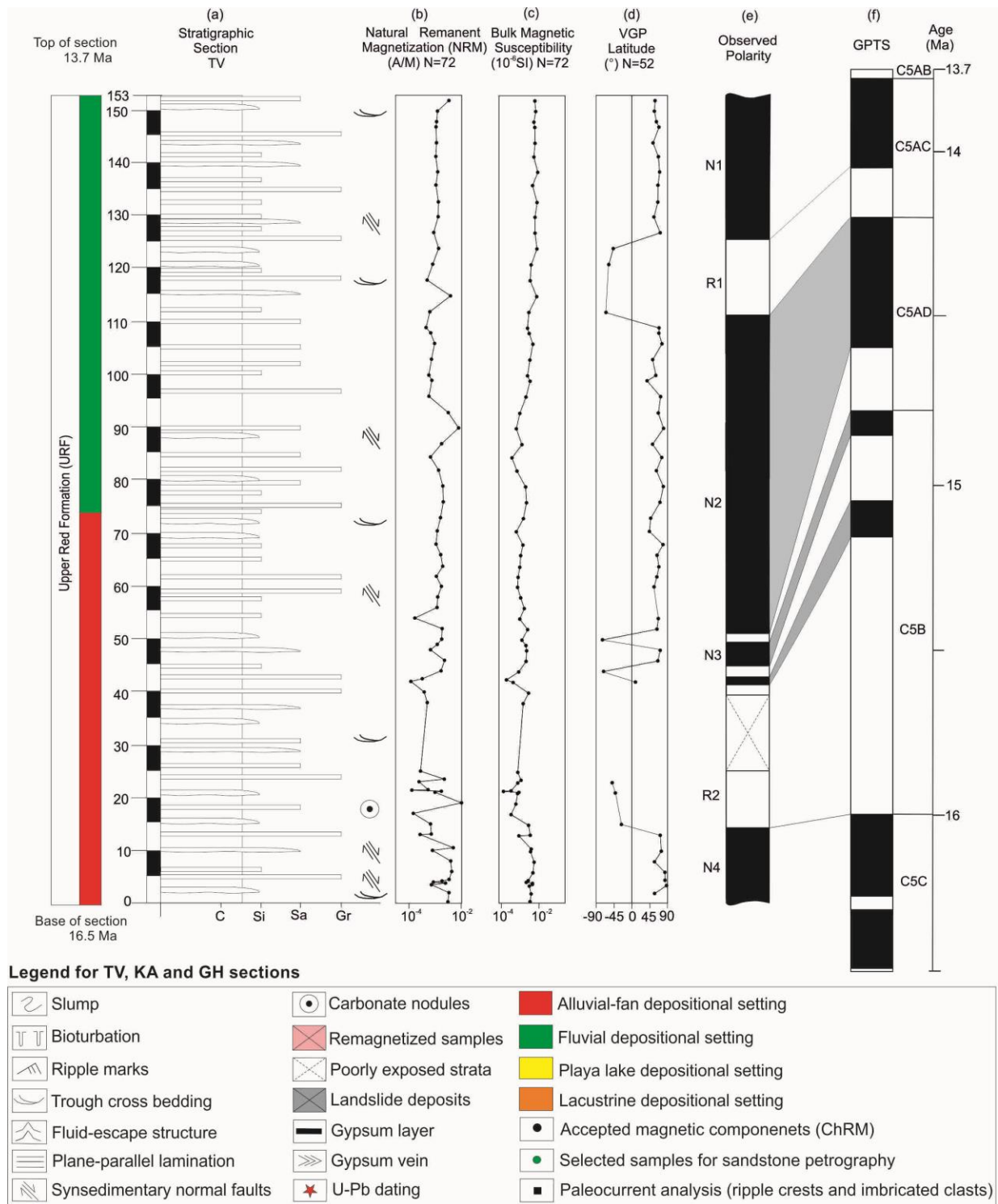
533

534

535

536

537

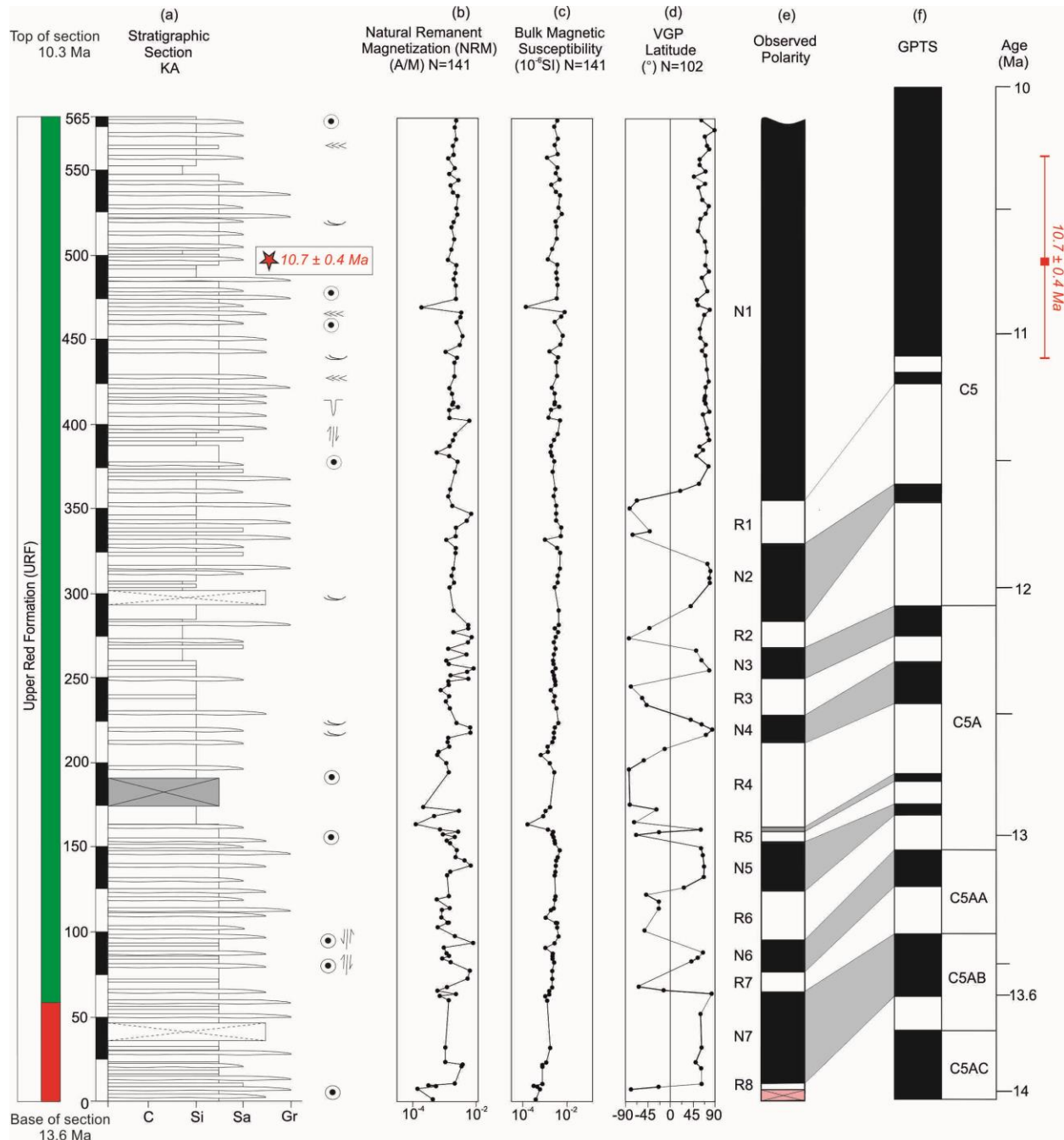


538

539 Figure 8. (a) Stratigraphic sections TV including (b) NRM (Natural Remnant Magnetization), (c) Bulk magnetic

540 susceptibility, and (d) VGP latitude (Virtual Geomagnetic Pole). The VGP latitudes were used for constructing (e)

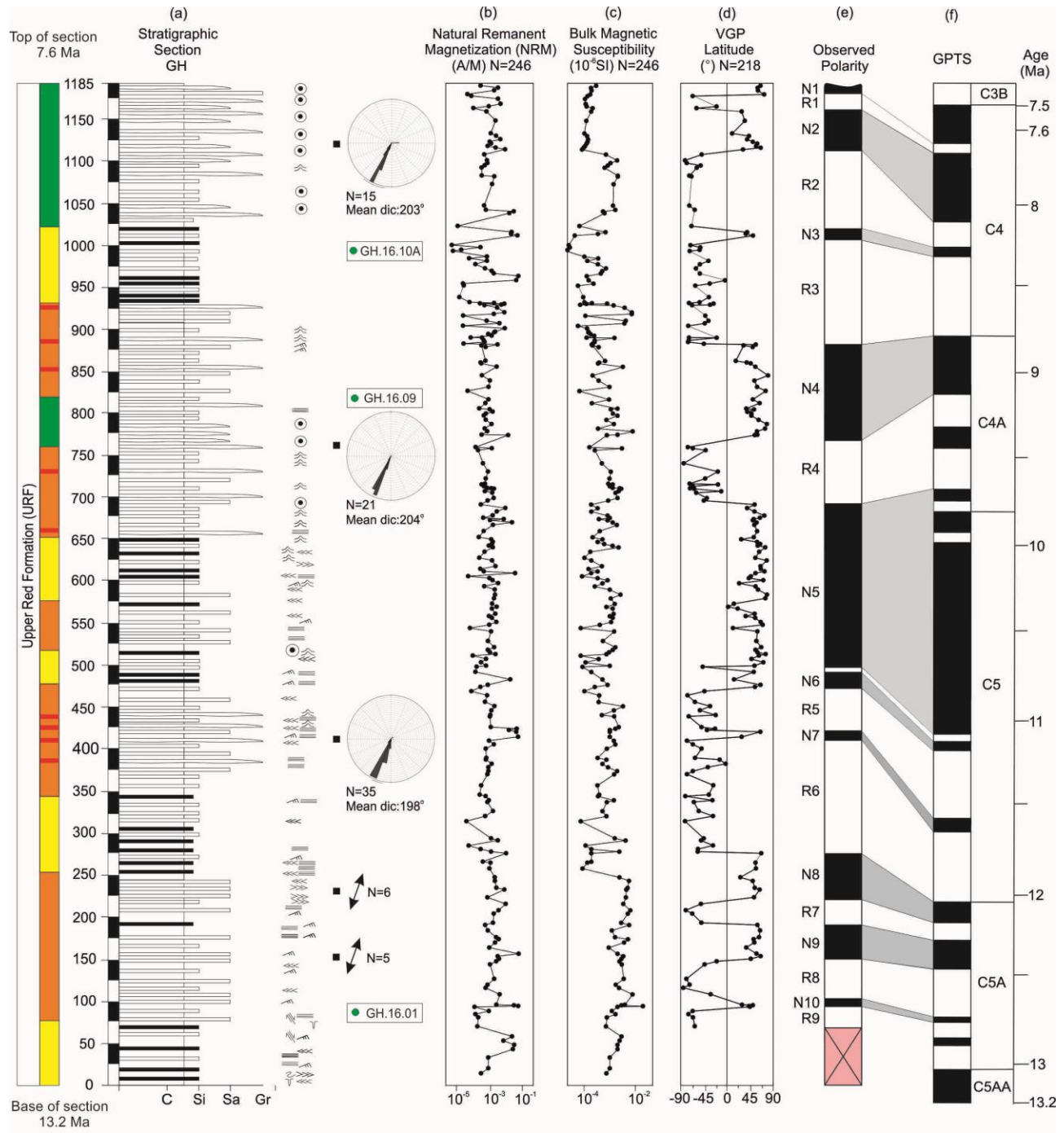
541 observed polarity scales, which were subsequently correlated each stratigraphic section with (f), the reference GPTS
 542 (geomagnetic polarity time scale) of Gradstein et al. (2012). Grey magnetozones of observed polarity scale were
 543 detected by means of only one sample



544
 545 Figure 9. (a) Stratigraphic sections KA including (b) NRM (natural remnant magnetization), (c) Bulk magnetic
 546 susceptibility, and (d) VGP latitude (virtual geomagnetic pole). The VGP latitudes were used for constructing (e)
 547 observed polarity scales, which were subsequently correlated each stratigraphic section with (f), the reference GPTS

548 (geomagnetic polarity time scale) of Gradstein et al. (2012). Grey magnetozones of observed polarity scale were
 549 detected by means of only one sample.

550
 551



552
 553 Figure 10. (a) Stratigraphic sections GH including (b) NRM (natural remnant magnetization), (c) Bulk magnetic
 554 susceptibility, and (d) VGP latitude (virtual geomagnetic pole). The VGP latitudes were used for constructing (e)

555 observed polarity scales, which were subsequently correlated each stratigraphic section with (f), the reference GPTS
556 (geomagnetic polarity time scale) of Gradstein et al. (2012). Grey magnetozones of observed polarity scale were
557 detected by means of only one sample

558

559 **4.2.4. Paleomagnetic tests**

560 To assess the primary nature of the isolated ChRM directions the reversal and fold tests were
561 performed using a Python script, based on the orientation matrix method of Tauxe & Watson
562 (1994). For each magnetostratigraphic section the bootstrap reversal test (Tauxe et al., 1991) has
563 been carried out separately. In the TV and KA sections the normal and reverse polarities
564 directions are antipodal and the reversal test is positive (Figure 7h). On the contrary in the GH
565 section the normal and reverse polarities are not antipodal and the bootstrap reversal test is
566 negative, suggesting that data population could be partially affected by a recent magnetic
567 overprint that was not completely removed during stepwise demagnetization (Figure 7h). The
568 fold test was carried out for all the ChRM directions from the three stratigraphic sections (in total
569 373 direction) in order to have significant differences in the bedding attitudes. The mean
570 direction of the entire dataset is better grouped after tectonic correction ($D = 7.5^\circ$; $I = 40.0^\circ$, $k =$
571 6.3 , $\alpha_{95\%} = 3.2^\circ$) rather than before ($D = 308.8^\circ$, $I = 74.2^\circ$, $K = 4.4$, $\alpha_{95\%} = 3.9$) (Figure 7g). At
572 the same time, the bootstrap fold test (Tauxe et al., 1991) is positive showing that the degree of
573 unfolding to produce the maximum τ_1 is between 86 and 106 % (Figure 7i). These results
574 demonstrate that the ChRM directions from the three stratigraphic sections were most likely
575 acquired before folding. Finally, it is worth to note that the mean ChRM direction obtained from
576 the three stratigraphic sections ($D = 7.5^\circ$; $I = 40.0^\circ$) is very similar to the one obtained from 14
577 sites from the same basin ($D = 10.2^\circ$; $I = 40.6^\circ$) with a positive reversal and fold tests (Mattei et
578 al., 2017). These data further support the primary origin of the ChRM in red beds of the URF as

579 also demonstrated by a recent paleomagnetic study in NE Iran (Mattei et al., 2019). On this basis
580 we are confident that our data allow determining correct polarities (latitude of the Virtual
581 Geomagnetic Poles, VGP) and hence to build up a reliable local magnetic polarity stratigraphy.

582

583 **4.3. Magnetostratigraphy**

584 The VGP latitudes from the new paleomagnetic data set define normal and reverse polarity
585 magnetozones (Figures 8e, 9e and 10e) and hence allow us to construct for each section a
586 magnetic polarity stratigraphy to be correlated with the Geomagnetic Polarity Time Scale
587 (GPTS) (Gradstein et al., 2012). In the following, we first correlate the KA section based on an
588 independent radiometric age, and then we correlate the underlying TV and the overlying GH
589 stratigraphic sections.

590

591 **4.3.1. KA stratigraphic section**

592 In the KA stratigraphic section 7 normal (N1-N7) and 8 reverse (R1-R8) polarity zones were
593 defined. A Zircon U-Pb age of 10.7 ± 0.4 Ma (Table 3) from an ash layer in the upper part of the
594 section at ~ 500 m suggests that the long-lasting normal polarity zone N1 should be correlated
595 with chron C5n1n. Consequently, the two short reverse polarity zones R1 and R2 and the longer
596 normal polarity zone N2 should belong to the same C5 chron. According to these correlations,
597 the polarity zones N3, N4, N5 as well as the reverse polarity zones R3, R4, R5 and R6 should
598 correspond to chron C5A. In the lower part of the section, the normal and reverse polarity zones
599 N6 and R7 can be correlated with chron C5AA, while the long lasting normal polarity (N7) and
600 the short reverse polarity zone at the base of the section can be correlated to chron C5AB. Based

601 on this correlation the most likely depositional age for the KA stratigraphic section will be
602 between ~ 13.6 to 10.3 Ma (Figure 9).

603

604 **4.3.2. TV stratigraphic section**

605 Patterns of VGP latitudes in section TV define 4 normal and 2 reverse polarity zones denoted as
606 N1-N4 and R1-R2, respectively. Stratigraphically, the TV section lies underneath the KA
607 stratigraphic section (Figure 2), thus we correlate the uppermost long normal polarity zone N1
608 and the reverse polarity zone R1 with chron C5AC. Consequently, the long normal polarity zone
609 N2 in the middle part of the section is correlated with chron C5AD and the short normal polarity
610 zone N3 with chron C5B. One reverse polarity zone in chron C5AD, one short normal as well as
611 a reverse polarity zone in the upper part of chron C5B in the GPTS are missing in our records.
612 Besides these three incompatibilities, which represent the time period between ca. 14.6 to 15.1
613 Ma, we successfully matched up each chron with the GPTS. We note that the missing chrons
614 come from the lower part of the section where the sedimentation rate is lower (~ 0.025 mm/yr)
615 (Figure 11) and the probability to miss a chron greater. The reverse polarity zone R2 in the
616 lowermost part of the section should correspond to chron C5B, while the long normal polarity
617 zone N4 at the base of the section should correlate with chron C5C. Accordingly, a depositional
618 age of ~ 16.5 to 13.7 Ma is proposed for the TV stratigraphic section (Figure 8).

619

620 **4.3.3. GH stratigraphic section**

621 Patterns of VGP latitudes in section GH define 10 normal and 9 reverse polarity zones, denoted
622 as N1-N10 and R1-R9, respectively. Stratigraphic sections KA and GH overlap, hence, in our
623 tentative correlation we associate the long-lasting, distinctive normal polarity zone N1 of section

624 KA with the normal zone N5 in the middle part of section GH. The uppermost normal polarity
625 zones N1, N2 and N3 as well as the short reverse polarity zone R1 and long-lasting reverse
626 polarity zones R2 and R3 at the top of the section can be correlated with chron C4.
627 Consequently, the normal and reverse polarity zones N4 and R4 correlate with chron C4A. The
628 long-lasting normal polarity zone N5 in the middle part of the section as well as the two short
629 normal polarity zones N6 and N7 and two long reverse polarity zones R5 and R6 correspond to
630 chron C5. Finally, the normal polarity zones N8, N9 and N10 and the reverse polarity zones R7,
631 R8 and R9 in the lowermost part of the section should correlate with chron C5A. Based on this
632 correlation the depositional age of section GH should range from ~ 13.2 to 7.6 Ma (Figure 10).
633 Combined our data document a depositional age for the red beds in Tarom Basin from ~ 16.5 to
634 at least 7.6 Ma. Importantly, this implies that these red clastics belong to the Upper Red
635 Formation.

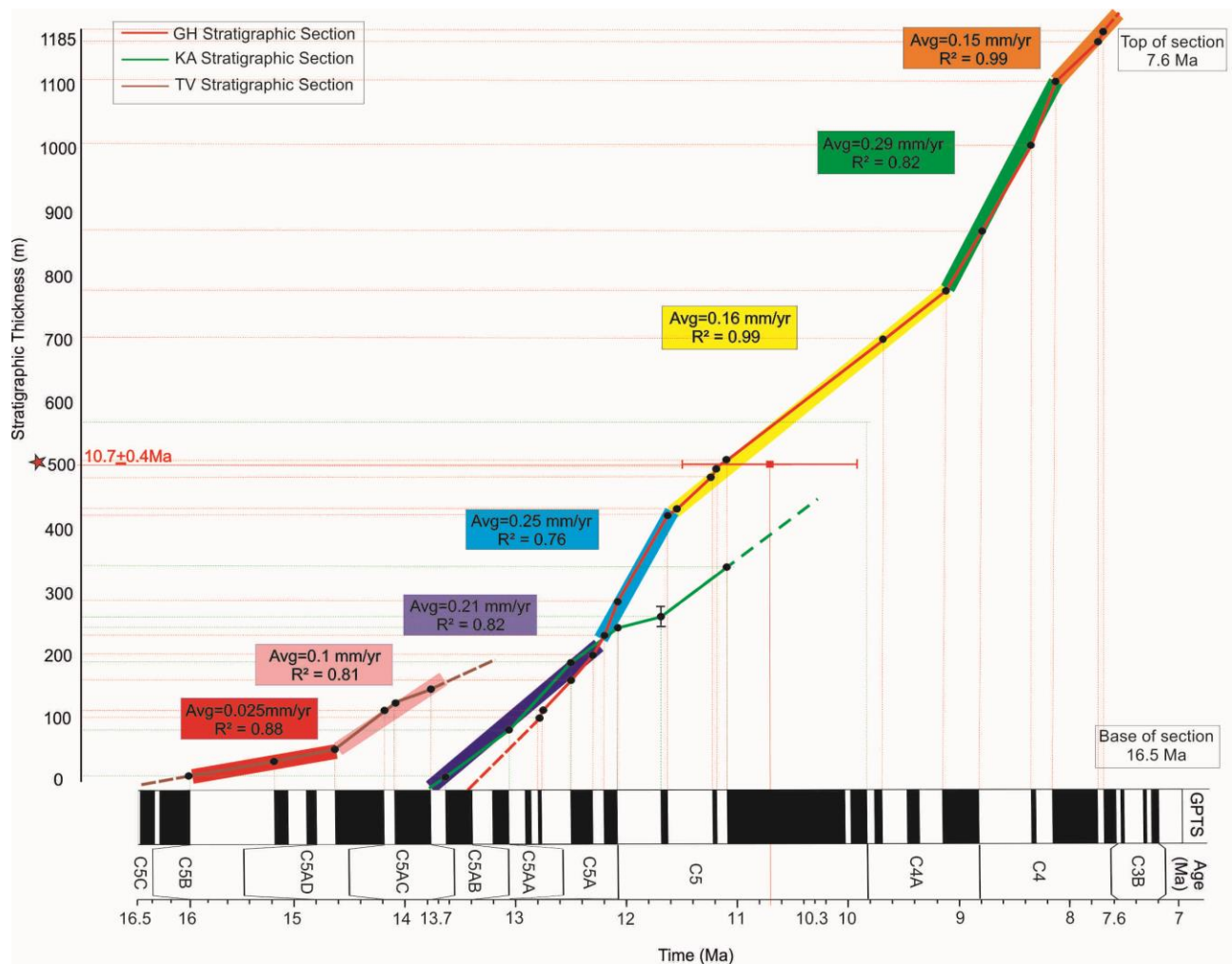
636

637 **4.4. Sediment accumulations rates**

638 The sediment accumulation rates for each stratigraphic section were calculated based on the
639 magnetostratigraphic correlations and the stratigraphic thickness measured in the field (Figure
640 11). The oldest record (from ~ 16.5 Ma) is from the TV section where rates are relatively low
641 (0.025 mm/yr) until ~ 14.6 Ma when an increase up to ~ 0.1 mm/yr occurs. From ~ 13.6 Ma the
642 record includes both the GH and KA sections with similar rates of ~ 0.21 mm/yr at least until \sim
643 12.1 Ma. By ~ 12.1 Ma, sediment accumulation rates for the GH section increase up to ~ 0.29
644 mm/yr and remain higher than those in the KA section (at least until the top of the KA section at
645 ~ 10.3 Ma). At the top the section, sediment accumulation rates decrease down to 0.15 mm/yr.
646 Overall, the sediment accumulation rates from the intermontane Tarom Basin are slightly lower

647 than those recorded in the Miocene foreland basins of N Iran (0.3 to 2.2 and 0.3 to 0.5 mm/yr for
 648 the southern Alborz Mountains and the Great Pari Basin, respectively; Ballato et al., 2008, 2017)
 649 but they are still comparable with rates observed in tectonically active regions of the Alpine-
 650 Himalayan orogenic belt (e.g., Charreau et al., 2005; Huang et al., 2006; Zhu et al., 2008; Chang
 651 et al., 2012).

652



653

654 Figure 11. Long-term sediment accumulation rates for the Miocene synorogenic sediments of the three investigated
 655 stratigraphic sections. Rates have been obtained by using a linear best fit model (see correlation coefficient R^2)
 656 according to the different segments shown with the colourful boxes

657

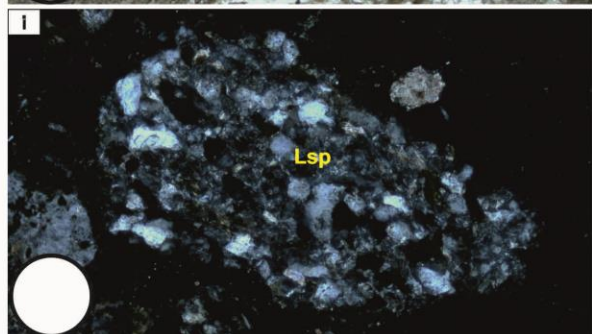
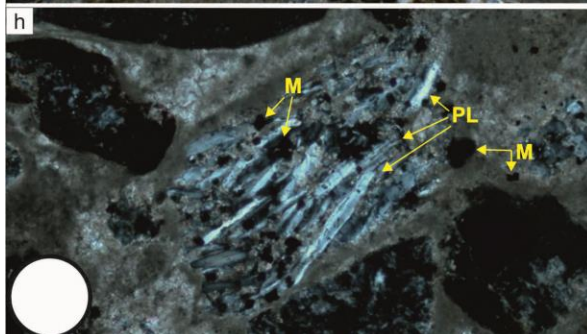
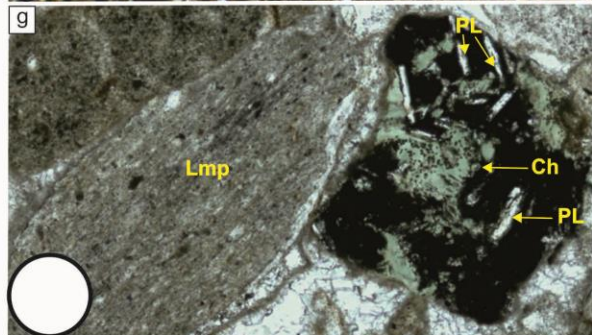
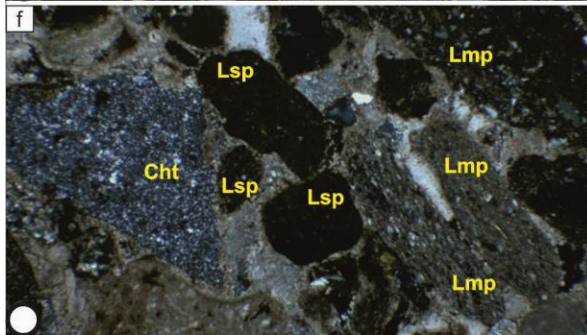
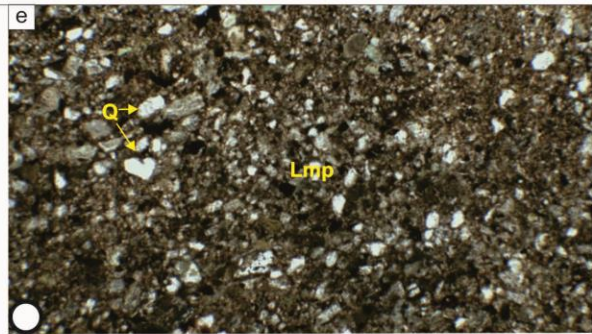
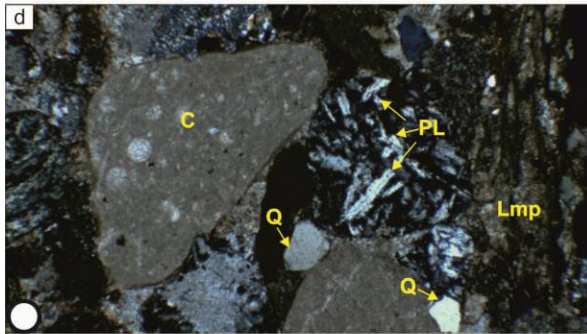
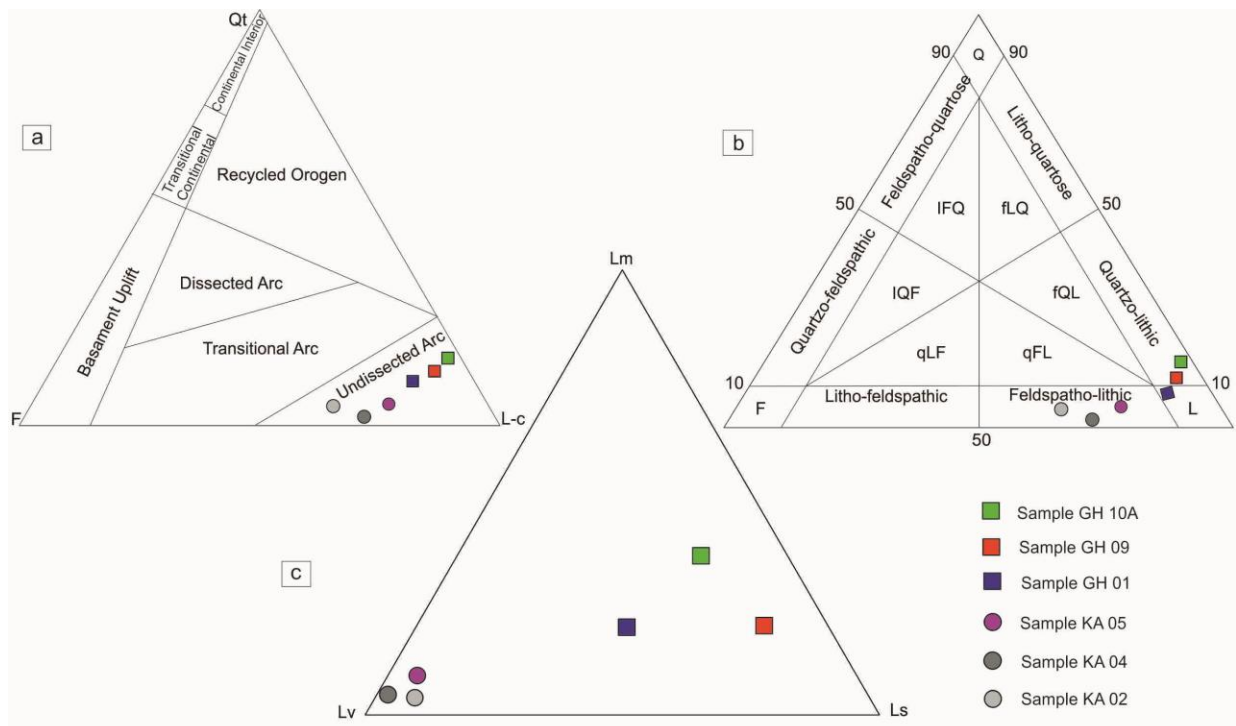
658 **4.5. Sandstone petrography**

659 Petrographic analyses were performed on 6 thin sections collected along the KA and GH
660 stratigraphic sections according to the Gazzi-Dickinson method (Ingersoll, et al., 1984). Results
661 are plotted on QFL-c, QFL and Lm-Lv-Ls ternary diagrams (Figures 12a-c, respectively,
662 Dickinson et al., 1985; Garzanti, 2019). A detailed table can be found in the Appendix (Tables
663 A3.1 and A3.2). The KA sandstones are rather homogenous and mainly composed of volcanic
664 mafic clasts (Lvm, 50 and 58%) and plagioclase (Pl) grains (Figures 12a, 12c, 12d, 12g and 12h).
665 These are more abundant in the lower part of the section (30 vs 19%). A few lithic meta felsic
666 particles (Lmv; 6 to 9%) as well as a small amount (less than 5%) of quartz and heavy minerals
667 (epidote) are the other constituents observed in the KA samples. Finally, a minor amount ($\leq 3\%$)
668 of lithic fragments such as lithic volcanic felsic (Lvf), lithic limestone (Lcc), lithic terrigenous
669 (Lp), lithic metasedimentary (Lms) and metabasalt lithic fragment (Lmb) were also observed.
670 Conversely, the GH sandstone samples contain a lower proportion of volcanic lithics, and a
671 higher proportion of low-grade metamorphic particles (Figures 12b, 12c, 12e, 12f and Table
672 A3.1).

673 The most abundant constituent of the framework components is represented by lithic
674 metasedimentary (Lms) clasts, which range upsection from 14 to 37% (Table 1). The second
675 most abundant constituents are lithic terrigenous (Lp; 8-25%). Other particles that are much
676 more abundant than in the KA samples are meta felsic (Lmv) and lithic limestone (Lcc) clasts (4
677 to 17% and 9 to 16%, respectively). Volcanic mafic clasts (Lvm) are less abundant than in the
678 KA samples and show a significant upsection decrease from 21 to 3%. Quartz (Figures 12e and
679 12i) and feldspar particles were also observed in GH sandstones (Figures 12d and 12h). Feldspar
680 grains are less abundant than in the KA samples, with plagioclase particles ranging from 3 to

681 10%, while the alkali feldspars display also a very small amount (1%). Instead, Quartz grains are
682 more abundant (9 to 13%). A minor amount ($\leq 3\%$) of other lithic fragments (Lvf, Lch, Lmf) and
683 heavy minerals (such as epidote) were also observed.

684 Overall, the abundance of volcanic clasts in the KA samples indicates that the main sediment
685 source along the southern margin of the basin must have been from the Eocene volcanics (Karaj
686 Formation) of the Tarom range. It should also be noted that while the thin sections from the KA
687 do not present any clasts of intrusive rocks, the unconformable conglomerates of supposed
688 Pliocene contains abundant clasts of granitoides, which are currently exposed along the southern
689 slope of the range (Figure 2). This indicates post 7.6 Ma exposure of the granitoides of the
690 Tarom range. Concerning the central sectors of the basin, the occurrence of metamorphic and
691 sedimentary lithics, as well as the progressive decrease in volcanic grains suggests that the
692 central sectors of the basin (GH samples) were mostly sourced from the northern basin margin
693 (Alborz Mountains). This agrees with paleocurrent directions obtained in different sectors of the
694 GH stratigraphic section (Figure 10).



696 Figure 12. QFL triangular diagrams with tectonic zones defined by (a) Dickinson, (1985) and (b) Garzanti, (2019).
 697 Q
 698 represents total quartz grains (Qm = monocrystalline and Qp = polycrystalline), F represents total feldspar grains (P
 699 = plagioclase and K-feldspars), L total lithic clasts and L-c: total lithic clasts excluding carbonates. (c) Lm-Lv-Ls
 700 ternary plot for the Tarom Basin (Lm = metamorphic; Lv = volcanic; Ls = sedimentary). (D to I) Representative
 701 photomicrographs of sandstone samples. (d) Sample GH-16-05 (stratigraphic position of ~ 410 m) showing a large
 702 calcareous grain (c), a volcanic mafic grain with plagioclases (PL), a slate fragment with rough cleavage (Lmp) and
 703 quartz grains. (e) Sample GH-16-04 (at ~ 370 m) with metamorphic clasts and quartz (Q) grains in a terrigenous-
 704 carbonatic matrix. (f) Sample GH-16-05 (at ~ 410 m) with chert (Cht), pelitic lithic (Lsp) and metamorphic
 705 fragments (Lmp). (g) Sample GH-16-10B (~ 990) showing a volcanic mafic grain (Lvm) with Pl altered in green
 706 Chlorite (Ch), and Lmp. (h) Sample KA-16-05 (~ 450) displaying a volcanic mafic grain with Pl and magnetite (M)
 707 crystals. (I) Sample GH-16-01 (~ 75 m) showing a sandy siltstone lithic fragment with detrital micas (Lsp). Note
 708 that all photos are under cross polarized light except figure f. Small and large white circles show scales of 4 and 10
 709 microns, respectively.

710

711 **5. Discussion and Conclusions**

712 Based on our new age determinations and the reconstruction of the depositional systems and
 713 sediment dispersal patterns we propose a four-stage evolutionary model for the Tarom Basin for
 714 the last ~38-36 Ma (Figure 13a-d) and we discuss the main implications of our findings for the
 715 lateral (orogen perpendicular) evolution of the IP, including the mechanisms that led to the
 716 growth of its northern margin (Figure 14).

717

718 **5.1. ~38-36-16.5 Ma: topographic growth of the southern margin, formation of angular 719 unconformities and development of external drainage conditions**

720 The geometrical relationships among the strata of the Karaj Formation exposed along the
 721 southern sectors of the Tarom Basin suggest that minor folding must have occurred during the

722 latest stages of Eocene arc volcanism around 38-36 Ma (Figures 3b and 6). This could represent
723 the earliest event of Late Eocene-Early Oligocene collisional deformation recorded across the
724 entire Arabia-Eurasia collision zone from the Zagros to the Caucasus, Talesh, Alborz and Koph
725 Dagh mountains (Vincent et al., 2007; Morley et al., 2009; Ballato et al., 2011, 2015;
726 Mouthereau et al., 2012; Rezaeian et al., 2012; Roberts et al., 2014; Tadayon et al., 2018).
727 Furthermore, our Middle-Late Miocene age of the overlying red beds indicates that the
728 topographic growth of the Taron range prevented the Late Oligocene-Early Miocene marine
729 transgression that led to the deposition of the shallow-marine sediments of the Qom Formation
730 (Figure 14a; e.g., Reuter et al., 2009). Therefore, between 38-36 Ma and ~ 16.5 Ma (initiation of
731 red beds sedimentation) the Taron Basin must have experienced external drainage conditions.
732 This implies that the eroded sediments were delivered directly to the Caspian Sea and hence a
733 connection between the Taron Basin and Caspian Sea must have been established after the end
734 of arc volcanism (Figure 14a). Sometime during this ~ 20-My-long period both basin margins
735 experienced tilting that led to the development of an angular unconformity between the Karaj
736 Formation and the overlying red beds (Figure 3). Prior to that, the Alborz Mountains represented
737 a topographic barrier between central Iran and the Caspian Sea as suggested by the lack of
738 Eocene volcanics along the northern slope of the Alborz (Figure 14a; Guest et al., 2006a).

739

740 **5.2. ~16.5 to < 7.6 Ma: intermontane basin development and internal drainage conditions**

741 Sedimentation of continental red beds in the Taron Basin started at ~ 16.5 Ma and lasted at least
742 until 7.6 Ma. This indicates that these sediments are stratigraphically equivalent to the Upper
743 Red Formation (e.g., Ballato et al., 2008, 2017). During that time interval sedimentation occurred
744 in an intermontane basin developed most likely as flexural response to tectonic loading from the
745 adjacent uplifting mountain ranges (Alborz Mountains to the N and Taron range to the S;

746 Figures 13b and 14a). Basin development was associated with a sharp increase in sediment
747 accumulation rates (one order of magnitude, from 0.025 to 0.21 mm/yr) along the TV section at
748 ~14.6 Ma (Figure 11). Furthermore, the occurrence of lacustrine and playa lake deposits in the
749 basin depocenter implies the development of internally drained conditions associated with the
750 topographic growth of the Alborz Mountains, which must have disconnected the former drainage
751 system from the Caspian Sea. Such a topographic growth was triggered by widespread regional
752 deformation related to a more advanced stage of the Arabia-Eurasia collision (e.g., Ballato et al.,
753 2011; Mouthereau et al., 2012) in agreement with available low-temperature thermochronology
754 data in NW Iran (Guest et al., 2006b; Rezaeian et al., 2012; Ballato et al., 2013, 2015;
755 Madanipour et al., 2013, 2017). This is further corroborated by the presence of growth strata
756 along the north margin of the basin indicating syndepositional contractional deformation
757 (Figures 2, 3e and 13b-d).

758 Our sediment provenance data provide additional information on to the evolution of the sediment
759 source area. The southern side of the basin received sediments from the growing Tarom range.
760 There, exhumation has been limited to less than 3-4 km as documented by available 41-32-My-
761 old apatite fission track ages that may still record magmatic cooling (Rezaeian et al., 2012). This
762 is also shown by the sandstone petrography data from the KA section, that have a rather constant
763 composition dominated by volcanic lithics and feldspars (feldspatho-lithic arenite; QFL plot;
764 Figure 12b), as expected for undissected arc regions (QtFL-c ternary diagram; Figure 12a).
765 Instead, the central part of the basin received a greater amount of sediments from the Alborz
766 Mountains as documented by the higher proportion of metamorphic lithics and quartz grains
767 (quartzo-lithic arenite; Figure 12b). Although these sample plot also in the undissected arc
768 (Figure 12a), the upsection increase in metamorphic grains and the relative decrease in volcanic

769 lithics suggests erosional unroofing with the progressive exposure of the metamorphic basement.
770 This agrees with a fully reset Miocene apatite fission track age (Rezaeian et al., 2012) indicating
771 that exhumation along the Alborz Mountains was greater than in the Tarom range.

772

773 **5.3. <7.6 Ma to Pliocene? drainage reintegration, basin uplift, deformation and erosion**

774 Sometime after ~7.6 Ma, the Tarom Basin was reintegrated into an external drainage system and
775 a new fluvial connection with the Caspian Sea developed. One possible cause could be fluvial
776 headward erosion triggered by the km-scale, base level drop of the Caspian Sea between ~ 5.5
777 and 3 Ma (Forte & Cowgill, 2013;). Alternatively, basin capture may have occurred through
778 overspill from the Tarom Basin into the Caspian Sea. In any case, after 4 Ma, the Tarom Basin
779 must have been integrated into the drainage system of the Qezwl-Owzan as documented by
780 overflow processes from the adjacent and more elevated Mianeh Basin of the Iranian Plateau that
781 led to the development of ~1-km-deep Amardos gorge (Figure 1; Heidarzadeh et al., 2017). The
782 establishment of an external drainage system appears to coincide with intrabasinal deformation,
783 basin uplift and erosion, as recorded by several post 7.6 Ma anticline-syncline pairs, in the
784 central sectors of the basin (Figures 2 and 3h). This is well visible in the central sectors of the
785 study area (GH section) where the occurrence of subvertical to overturned red beds suggests the
786 development of a north verging anticline most likely associated with a detachment horizon
787 within gypsum layers at the base of the red beds.

788

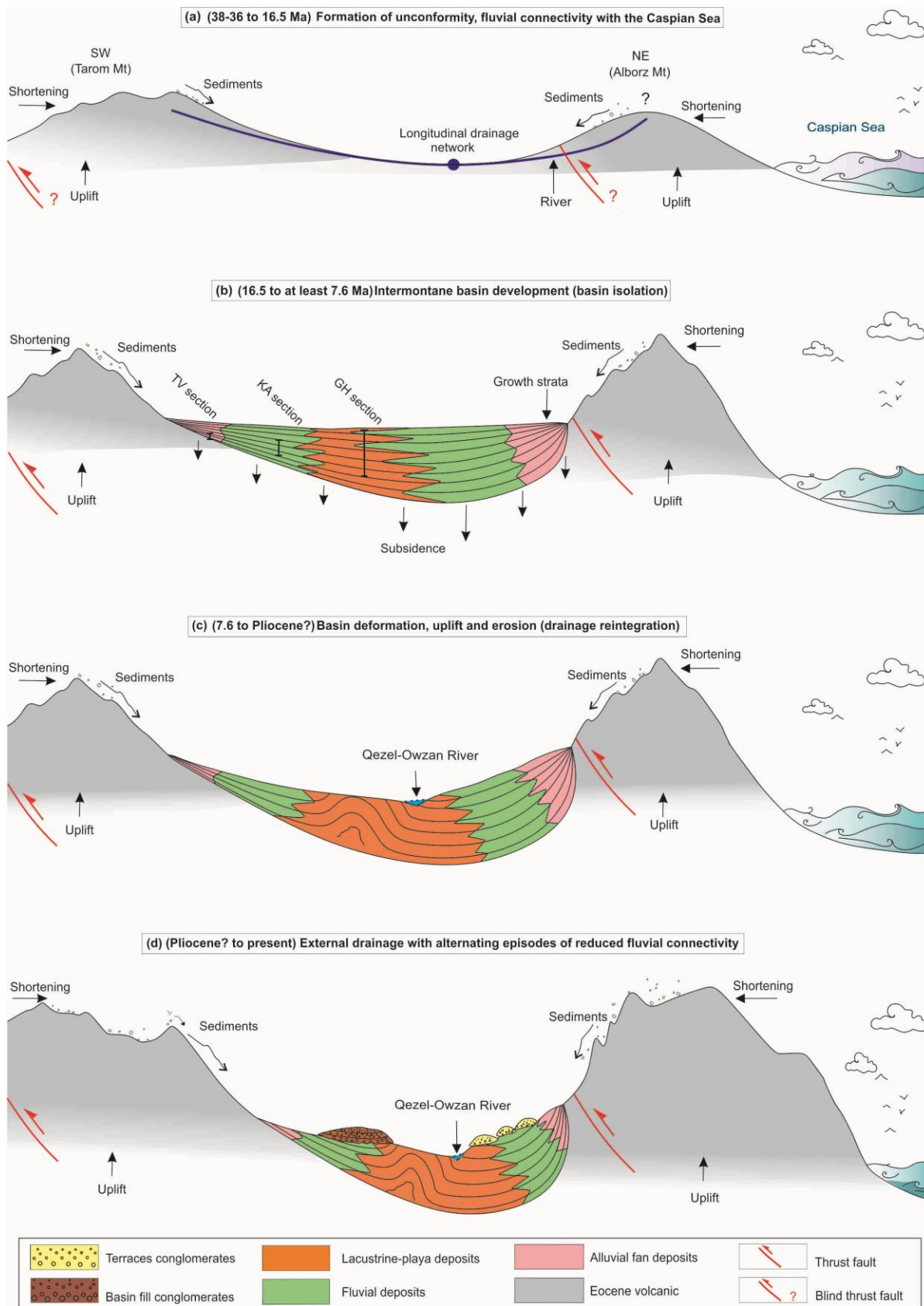
789 **5.4. Pliocene? to Present: alternating episodes of basin aggradation, incisions and** 790 **excavation**

791 Following intrabasinal deformation, the Tarom Basin experienced at least one major episode of
792 (supposed) Pliocene conglomerate deposition (Stocklin, 1969; Figure 3a) as well as three main

793 phases of basin aggradation and incision, as documented by distinct levels of Quaternary terrace
794 conglomerates (Figures 2, 3a and 13d). These unconformable deposits suggest the occurrence of
795 alternating phases of limited (or absent) and efficient fluvial connectivity with the Caspian Sea.
796 A similar configuration has been described in the intermontane basins of arid to semiarid
797 climatic regions like those forming the Eastern Cordillera and the broken foreland of NW
798 Argentina. There, the landscape response to Quaternary climate changes is thought to be the
799 main driver of short-term cycles (10^5 years) of basin filling and excavation, while tectonics plays
800 a major role in controlling the long-term filling history (10^6 years; Strecker et al., 2009; Streit et
801 al., 2015; Schildgen et al., 2016; Tofelde et al., 2017; Ballato et al., 2019; Pingel et al., 2019).
802 Here, the lack of chronological constraints does not allow unravelling the role of different
803 forcing mechanisms. In any case, it should be noted that, the supposed Pliocene conglomerates
804 are slightly folded into a broad syncline suggesting a possible interplay between intrabasinal
805 deformation and sedimentary loading/unloading cycles, which can hinder/promote intrabasinal
806 deformation (Ballato et al., 2019). For example, these conglomerates are in unconformity onto
807 folded Miocene red beds, therefore, their deformation must have occurred after their deposition
808 either during or after their removal through fluvial erosion (i.e., during sedimentary unloading).
809 Finally, it should be noted that a similar long-term, tectono-stratigraphic history has been
810 proposed for the intermontane Taleghan-Alamut basin of the central-western Alborz Mountains
811 (Guest et al., 2007). There, the deposition of Middle-Late Miocene red beds was followed by
812 Late Miocene-Pliocene intrabasinal deformation, Pliocene aggradation with conglomerate
813 deposition and Quaternary fluvial incision. This common evolution suggests that the orogen may
814 have responded along strike in a similar way to (either tectonic or climatic) forcing mechanisms
815 (Ballato et al., 2015).

817

818



820 Figure 13. Schematic diagram showing the Late Cenozoic evolution of the Tarom Basin (a) ~38-36-16.5 Ma, uplift
821 and tilting, formation of angular unconformities, and development of an external drainage system flowing into the
822 Caspian Sea. (b) ~ 16.5-7.6 Ma, basin isolation and internal drainage conditions, development of an intermountain
823 basin, uplift of the basin-bounding mountain ranges (Tarom and Alborz ranges). The red bars show the location of
824 three measured stratigraphic sections (c) ~7.6 Ma-Pliocene? drainage reintegration with renewed fluvial connectivity
825 with the Caspian Sea, intrabasinal deformation, basin uplift and erosion. (d) Pliocene? to present, cycles of incision
826 and aggradation, folding of basin fill conglomerates.

827

828 **5.5. Implications on plateau building processes**

829 Our multidisciplinary dataset provides new insights into the lateral (orogen perpendicular)
830 development of the Iranian Plateau and the vertical growth of its northern margin (Tarom range).
831 The hinterland of IP recorded foreland sedimentation starting from ~ 16.5 Ma, shortly after the
832 Late Oligocene-Early Miocene marine transgression that led to the deposition of the Qom
833 Formation (Ballato et al., 2017; Figure 14a). This implies that plateau uplift must be younger
834 than ~ 16.5 Ma. Flexural subsidence was triggered by mountain building processes along the
835 plate suture zone as documented by early Miocene low-temperature thermochronology data from
836 the Sanandaj-Sirjan Zone (Francois et al., 2014; Barber et al., 2018). Foreland basin initiation in
837 the plateau interior coincided with the development of the endorheic Tarom Basin and hence
838 with Middle Miocene topographic growth along the northern sectors of the Arabia-Eurasia
839 collision zone (Ballato et al., 2011, 2013, 2015; Rezaeian et al., 2012). Such a configuration
840 indicates that the retroforeland basin of the Arabia-Eurasia collision zone was partitioned into a
841 broken foreland, like in the North American Cordillera and the South American Andes (e.g.,
842 Jordan & Allmendinger 1986; Strecker et al., 2012). The retroforeland was compartmentalized
843 after ~ 11 Ma (Ballato et al., 2017) through the growth of few, orogen parallel, mountain ranges
844 in the plateau interior, which appear to have a regular wavelength of 40-50 km (Figures 14b and

845 14c). This led to the development of few internally drained intermontane basins and eventually
846 of a typical low-relief plateau morphology (Sobel et al., 2003; Garcia Castellanos et al., 2007),
847 that is still preserved in the sectors of the plateau that are internally drained (Figure 1).
848 Interestingly, while uplift in the broken foreland of the Andes occurred through the reactivation
849 of steep basement faults (Sierra Pampeanas; e.g., Jordan & Allmendinger 1986) or listric reverse
850 faults (Santa Barbara System; e.g., Kley & Monaldi, 2002) that extend up to at least ~ 25 km of
851 depth (Alvarado et al., 2007; Richardson et al., 2012), the IP presents a more complex pattern of
852 deformation and a shallow seismicity (maximum depth of 20 km, with the majority of the
853 hypocenters around 10 km; Maggi et al., 2002). Although a clear structural model for the IP is
854 currently missing, there are no evidences for a dominant vergence toward the upper plate with a
855 lower crust décollement rooted into the plate boundary as documented in the Altiplano and Puna
856 plateaus (e.g, Horton et al., 2018). A possible reason could be that Iran represents a mobile
857 orogenic belt (e.g., Faccenna et al., 2010) where different microplates were accreted and sutured
858 from the early Triassic (Zanchi et al., 2009; Wilmsen et al., 2009). This has produced some
859 peculiar characteristics such as: 1) the occurrence of orogenic sutures and several crustal scales
860 anisotropies that were repeatedly reactivated under extensional (Late Jurassic and Eocene; e.g.,
861 Brunet et al., 2003; Zanchi et al., 2006; Verdel et al., 2011) and compressional (Late Cretaceous
862 to Paleocene and latest Eocene to Oligocene; Guest et al., 2006; Zanchi et al., 2006; Yassaghi &
863 Madanipour, 2008; Rezaeian et al., 2012; Madanipour et al., 2017) regimes before widespread
864 Miocene collisional deformation (e.g., Ballato et al., 2011, 2013; Mouthereau et al., 2012); 2) the
865 presence of a composite stratigraphy (Figure 14b) with few episodes of accelerated subsidence
866 along different depocenters that led to the deposition of several km-thick clastic (the Late
867 Triassic, Shemshak Formation; e.g., Wilmsen et al., 2009; the Miocene, Upper Red Formation,

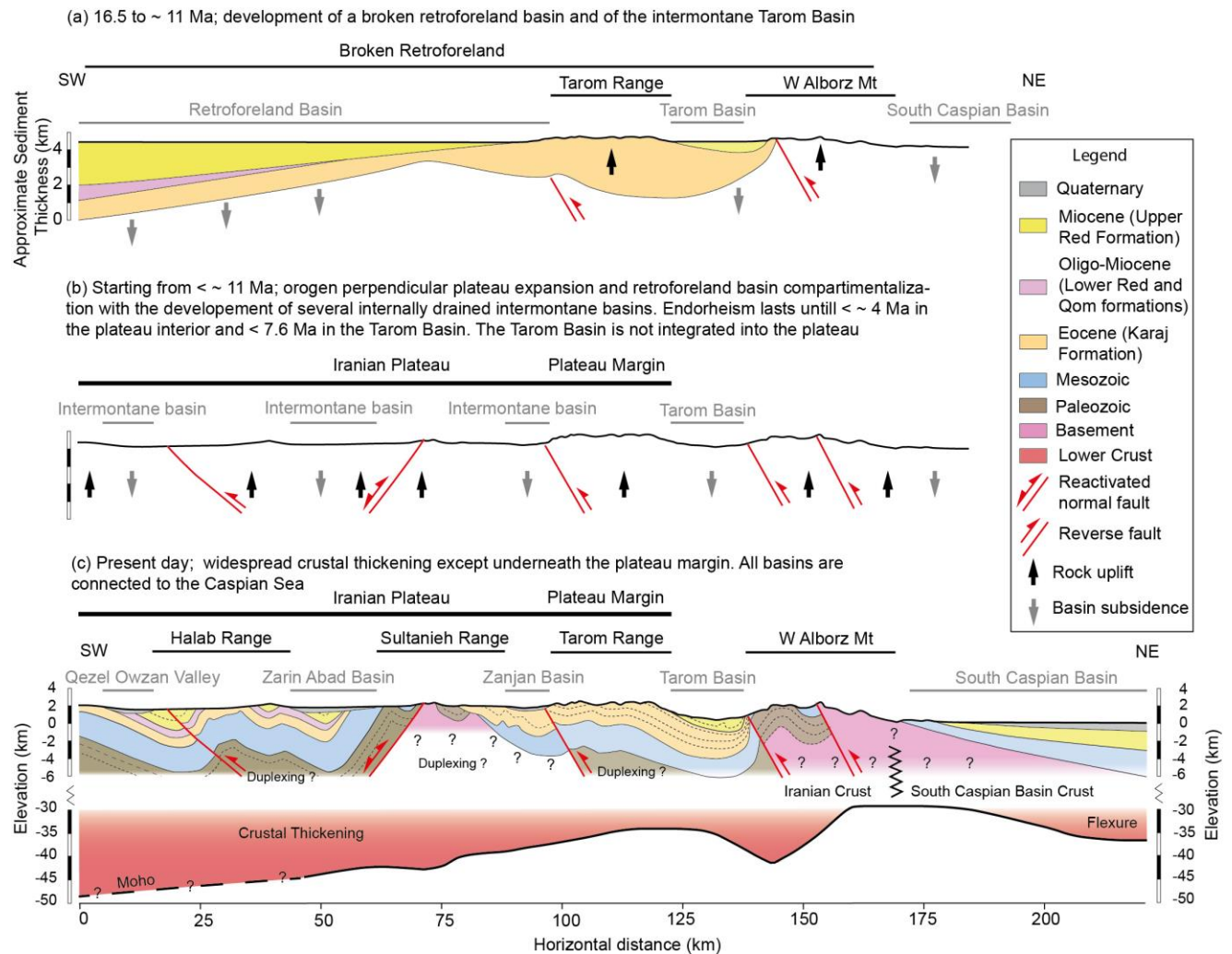
868 e.g., Ballato et al 2017) and volcanoclastic (the Eocene Karaj Formation; Verdel et al., 2011)
869 sedimentary sequences; 3) the occurrence of a warm lithosphere associated with Eocene
870 magmatism that continued in several sectors of the IP until the present (e.g., Chiu et al., 2013;
871 Rabiee et al., 2020).

872 During the growth of the IP margin, the Tarom Basin recorded continues syntectonic
873 sedimentation at least until ~ 7.6 Ma with the accumulation of more than ~ 1.2 km of red clastics.
874 Low-temperature thermochronology data document an acceleration in fault-related exhumation
875 along both margins of the Tarom Basin starting from 12-10 Ma (Rezaeian et al., 2012;
876 Madanipour et al., 2017), in agreement with our sediment accumulation rates. At the same time,
877 our sandstone petrography data suggest that the Alborz Mountains experienced a greater
878 magnitude of exhumation than the Tarom range. This implies that topographic growth in the
879 Tarom range was associated with limited erosional exhumation, as also documented by the
880 occurrence of subdued topography overlapped by basin-fill units in the plateau interior
881 (Heidarzadeh et al., 2017). This suggests that most of the Miocene convergence within the upper
882 plate must have been absorbed via crustal shortening and thickening in the western Alborz
883 Mountains and in the plateau interior rather than along its northern margin. This agrees with a
884 recent seismological study indicating a Moho depth of at least 45 km in the plateau interior that
885 tapers northward to ~ 35 km underneath the northern plateau margin and the Tarom Basin, and
886 increase up to 40-45 km beneath the western Alborz (Figure 14c; Motaghi et al., 2018).
887 Importantly, the occurrence of a ~ 35 km-deep Moho beneath the Tarom range, which is more
888 elevated than the thickened plateau interior, suggests that crustal shortening and thickening
889 cannot be responsible for the topographic growth of the plateau margin. Therefore, surface uplift
890 along the Tarom, must have been triggered by deep-seated, mantle driven processes (e.g.,

891 Hatzfeld & Molnar, 2010) rather than crustal/lithospheric shortening and thickening (e.g., Sobel
892 et al., 2003). One possible cause could be the removal of a thickened lithospheric mantle
893 sometimes between 12 and 10 Ma, when deformation processes appears to have accelerated
894 across Northern Iran (Hatzfeld & Molnar, 2010; Francois et al., 2014), and widespread uplift
895 seems to have occurred in the plateau interior (Figure 14b; Ballato et al., 2017). This agrees with
896 the occurrence of a thin lithospheric mantle across most of the upper plate (Rahmani et al., 2019,
897 and references therein), from the suture zone to the Caspian Basin. In any case, although
898 paleoaltimetric data are not yet available and therefore there are not constraints on the vertical
899 growth of the plateau, our reconstruction shows that: 1) the lateral (orogen perpendicular)
900 expansion of the plateau must have occurred over the last 11 Ma, and 2) by 11 Ma the IP must
901 have reached a lateral size similar to present-day one.

902 Finally, the reconstruction of the basin fills history of the Tarom Basin and our field observations
903 do not indicate the presence of elevations like those attained by the intermontane basins of the
904 plateau interior. This shows that the Tarom Basin was never incorporated into the IP during its
905 phases of internal drainage or limited connectivity with the Caspian Sea. Such a conclusion
906 agrees with a shallow Moho beneath the Tarom Basin (Figure 14c) and corroborates the idea that
907 topographic ponding

908



909

910 Figure 14. (a and b) Schematic reconstruction of the Late Cenozoic, broken, retroforeland basin of the Arabia

911 Eurasia collision zone during the orogen perpendicular expansion of the Iranian Plateau (see text for details). (c)

912 Geologic cross section (see figure 1 for location) based on Stocklin & Eftekharneshad, (1969), Davies (1977) and

913 our field observations, and Moho depth (solid line) from Motaghi et al., (2018). The dashed line is extrapolated from

914 the trend in crustal thickness across the IP shown in Rahmani et al., (2019).

915

916 5.6. Conclusions

917 Our work represents the first detailed study in the Taron Basin, an intermontane basin at the

918 transition between the Iranian Plateau and the Alborz Mountains. Combined, our data show that

919 the regional, Eocene arc volcanism in this area ended at ~ 38-36 Ma in association with the onset

920 of low-magnitude compressional deformation. This was followed by a prolonged phase of
921 erosion with development of angular unconformities. By ~16.5 Ma, the topographic growth on
922 the northern side of the basin (western Alborz Mountains) must have disconnected the Tarom
923 Basin from the Caspian Sea, leading to the formation of an internally drained intermontane basin.
924 Our new ages document that the synorogenic deposits of the Tarom range are stratigraphically
925 equivalent to the Miocene Upper Red Formation. The accommodation space available for
926 sedimentation was most likely controlled by lithospheric flexural in response to tectonic loading
927 of the adjacent mountain ranges. Internal drainage conditions lasted at least until ~7.6 Ma, when
928 basin incision and excavation occurred in association with intrabasinal deformation.
929 Subsequently the occurrence of supposed Pliocene conglomerates and at least three Quaternary
930 terrace conglomerates indicate multiple phases of aggradation and incision. This cyclic
931 behaviour occurred during alternating episodes of reduced and renewed fluvial connectivity with
932 the Caspian Sea. The lack of a detailed chronology, however, does not allow understanding the
933 forcing mechanisms for these cycles. In any case, the elevation of the Tarom Basin during
934 endorheic conditions did not reach those one of the plateau interiors, therefore, the basin was not
935 morphologically integrated into the IP. Furthermore, our reconstruction indicates that the plateau
936 was built on the broken retroforeland of the Arabia-Eurasia collision zone. Specifically, a
937 retroforeland basin developed starting from ~16.5 Ma during tectonic loading and topographic
938 building along the plate suture zone. This coincided with topographic growth along the northern
939 sectors of the collision zone and the development of the intermontane Tarom Basin. Starting
940 from ~11 Ma, intraforeland uplift led to the compartmentalization of the basin with the growth
941 of several mountain ranges over a typical wavelength ~40-50 km and intervening endorheic
942 intermontane basins. During this process the plateau reached a lateral size (orogen perpendicular)

943 like the present one. The northern margin of the IP (Tarom Range) experienced limited erosional
944 exhumation and crustal thickening, suggesting that the vertical growth of the plateau must have
945 been triggered by deep-seated processes (delamination of thickened lithospheric mantle?) rather
946 than crustal shortening and thickening, possibly by 12-10 Ma when upper plate deformation
947 accelerated.

948

949 **Acknowledgments**

950 This study is part of the PhD thesis of MP at the University of Roma Tre (PhD program Cycle
951 XXXII) and was supported by the PhD School of Roma Tre, the MIUR (Ministry of Education
952 University and Research; Grant Rita Levi Montalcini to PB), the DFG (German Science
953 Foundation; grants DFG BA 4420/2-1 and BA 4420/2-2 to PB) and the DAAD (German
954 Academy Research Service, grant to GH). The authors declare no financial or other conflicts of
955 interest. Software and analyzed data of paleomagnetic samples used to produce the results in this
956 work are available at
957 <https://data.mendeley.com/drafts/n5z4h9dy6x/DOI:10.17632/n5z4h9dy6x.2>.

958 The authors would like to thank Masoud Biralvand and Mahmood Fallah for helping with the
959 logistic during the field work.

960

961 **Appendix**

962 In the following we provide a detailed description of the analytical procedures for each
963 methodology used in this thesis. The raw data can be found in form of tables and figures.

964 A1. Zircon U-Pb-dating

965 A2. Zircon U-Pb-dating

966 A3. Sandstone petrography

967

968 **A1. Zircon U-Pb-dating**

969 Mineral separation was performed according to standard techniques (crushing, sieving, water
970 table, magnetic separation and heavy liquids as needed) at the Institute of Earth and
971 Environmental Science of the University of Potsdam. Zircons grains were sent to the the
972 Geochronology Laboratory in the Department of Earth and Space Sciences, University of
973 California Los Angeles for the sample preparation and the laboratory measurements. Epoxy
974 grain mounts of hand-selected zircons were gently ground to expose grain interiors and were
975 given final polish with 1 μm diamond. After ultrasonic cleaning, grains were surveyed for
976 internal compositional zonation and/or inclusions via cathode luminescence (CL) imaging.
977 Mounts were then coated with $\sim 100\text{\AA}$ of Au. U-Pb ages were determined based on U, Pb, and Th
978 isotopic spot measurements using the UCLA CAMECA ims 1270 ionprobe following the
979 analytical procedure explained in Schmitt et al. (2003). Each analytical run collected data for ten
980 cycles, and age calculations were performed by means of ISOPLOT (Ludwig, 2003). The final
981 ages listed in Table 3 of chapter 2 represent the weighted mean at the 95% confidence level for a
982 given number of aliquots ranging from two to seven (Figure A1.1; Mahon, 1996).

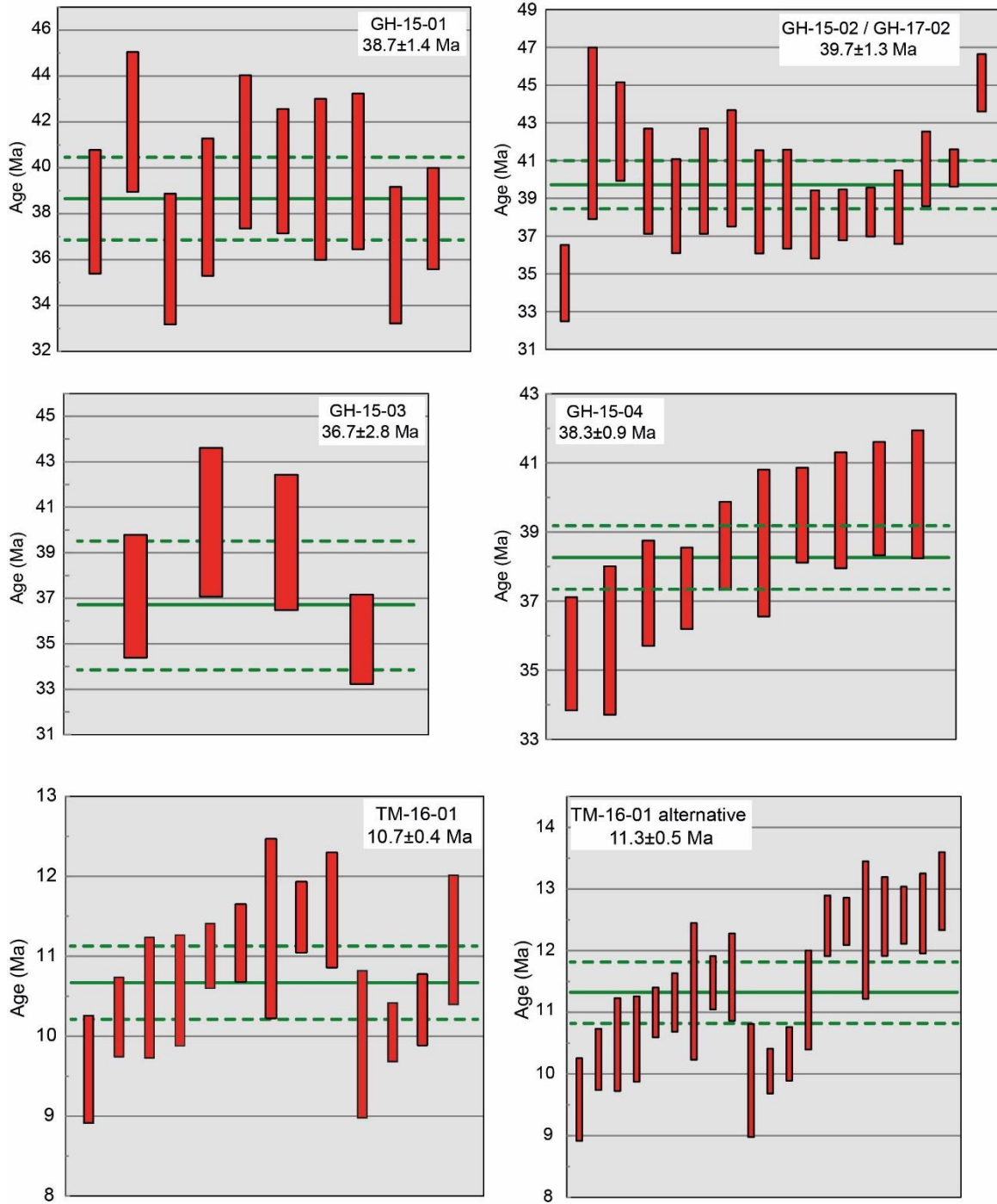
983

984 **References**

985 Ludwig, K.R. (2003). User's Manual for Isoplot/Ex, A geochronological toolkit for Microsoft
986 Excel Berkeley Geochronology Center Special Publication, v. 4, Berkeley Geochronology
987 Center, 2455 Ridge Road, Berkeley, CA 94709, USA.

988 Schmitt, A.K., Grove, M., Harrison, T.M., Lovera, O.M., Hulen, J. & Waters, M. (2003). The
989 Geysers–Cobb Mountain magma system, California (Part 1): U-Pb zircon ages of volcanic rocks,

990 conditions of zircon crystallization and magma residence times. *Geochimica et Cosmochimica*
 991 *Acta*, 67, 3423–3442.



993 Figure A1: Weighted averages for the analyzed samples shown with a green lines and associated error (in two
994 sigmas) in a dashed green line. The red boxes display the raw data of selected grains (2 sigma error). For sample
995 TM-16-01, two possible solutions are shown (see section 4.1; geochronology for details).

996

997 **A2. Zircon U-Pb-dating**

998 A total of 536 oriented samples were collected from the three investigated stratigraphic section
999 (TV, GH and KA section) for a combined stratigraphic thickness of 1185 m. The mean sampling
1000 interval is typically ~ 3m with at least two cores at each site. In case of poor outcrop conditions
1001 or in sectors composed mostly of coarse-grained sediments the sampling intervals was as large as
1002 ~ 5-6 m. All the samples were cored with a portable gasoline-powered drill. The orientations of
1003 the cores were measured by using a magnetic compass to determine both azimuth of core axis
1004 (declination) and dip of the core axis (inclination) and also corrected for ~ 5° E present day
1005 declination using magnetic field calculators (www.ngdc.noaa).

1006 Magnetic measurements were then performed using a 2-G Enterprises superconducting rock
1007 magnetometer equipped with DC-SQUID coils within a magnetically shielded room at the
1008 Alpine Laboratory of Paleomagnetism (ALP) at Peveragno (Turin) and at the INGV Laboratory
1009 of Paleomagnetism (Rome, Italy) shielded room in Rome, both in Italy. After measuring the
1010 Normal Remanent Magnetization (NRM), samples were subjected to stepwise (up to 15 steps)
1011 thermal demagnetization, using heating routine increments (150°C up to a temperature of 480°C
1012 and 30–50°C increments above 480°C) until the signal decreased below the instrumental
1013 detection limit or random changes of the paleomagnetic directions occurred. A set of sister
1014 specimens were chosen for AF demagnetization. Stepwise alternating field (AF)
1015 demagnetizations were done using a three-axis demagnetizer with a maximum field of up to
1016 100/120 mT, coupled with a 2G–DCSQUID magnetometer. Data processing was conducted by

1017 means of Rema soft program and led to the isolating the stable polarity directions of the
 1018 characteristic remanent magnetization (ChRM) by using the principal component analysis
 1019 (Kirschvink, 1980), data statistical analysis by means of Fisher statistics (Fisher, 1953), and
 1020 finally the calculation of the Virtual Geomagnetic Pole (VGP) from the ChRM vectors.

1021
 1022 **References**

1023 Fisher, R.A. (1953). Dispersion on a sphere, Proceedings of the Royal Society of London, Series
 1024 A, 217, 295–305.
 1025 Kirschvink, J.L. (1980). The least-squares line and plane and the analysis of palaeomagnetic
 1026 data, Geophysical Journal of the Royal Astronomical Society, 62, 699-718.

1027
 1028 **A3. Sandstone petrography**

1029 Six sandstone samples collected from the KA and GH sections in the Tarom basin were analyzed
 1030 under a polarized microscope in transmitted light (Table A3.1). In each sample, 400 points were
 1031 counted by using the Gazzi-Dickinson method (Ingersoll et al. 1984) the results of the modal
 1032 analysis are plotted in the ternary diagrams of Garzanti (2019) and Dickinson (1985) in order to
 1033 identify the local tectonic setting and the sediment provenance area (Table A3.1 and Table
 1034 A3.2).

1035
 1036 **Table A3.1**

1037 *Sandstone composition of the KA and GH stratigraphic studied sections in the Tarom Basin*

Sample Number	QFL; Garzanti (2019)			QtFL-c; Dickinson (1985)		
	Q	F	L	Qt	F	L-c
KA-16-02	5	31	64	4	32	64
KA-16-04	1	27	72	1	27	72
KA-16-05	5	20	75	5	20	75
GH-16-01	9	10	81	13	12	75
GH-16-09	11	5	83	15	7	78

GH-16-10A	13	4	83	15	4	81
-----------	----	---	----	----	---	----

1038 *Note.* (1) QFL by Garzanti (2019); (Q) Total quartz grains (Qm = monocrystalline + Qp = polycrystalline), (F):
 1039 Total feldspar grains (P = plagioclase + K-feldspars), (L) Total lithic fragments. (2) QtFL- by Dickinson (1985);
 1040 (Qt) Total quartzose grains (Qm + Qp), (F) Total feldspar grains (P + K), L-c: Total lithic fragments (excluding
 1041 carbonates).

1042 **Table A3.2**

1043 *Lm-Lv-Ls ternary plot for the Tarom basin*

Sample Number	Lm	Lv	Ls
KA-16-02	5	89	6
KA-16-04	6	93	1
KA-16-05	7	88	5
GH-16-01	20	39	41
GH-16-09	20	13	67
GH-16-10A	36	17	47

1044 *Note.* (Lm = metamorphic; Lv = volcanic; Ls = sedimentary)

1045

1046 **References**

1047 Dickinson, W.R. (1985). Interpreting provenance relations from detrital modes of sandstones. In:
 1048 Zuffa, G.G. (Ed.), Provenance of arenites. Reidel, Dordrecht, NATO ASI Series, 148, 333–361.
 1049 Garzanti, E.D. (2019). Petrographic classification of sand and sandstone. *Earth-Science Reviews*,
 1050 192, 545–563.
 1051 Ingersoll, R.V., Bullaed, T.F., Ford, R.L., Grimm, J.P., Pickle, J.D. & Sares, S.W. (1984). The
 1052 effect of grain size on detrital modes: a test of the Gazzi–Dickinson point-counting method.
 1053 *Journal of Sedimentary Petrology*, 54, 103 –116.

1054

1055

1056

1057

1058

1059

1060

1061

1062

1063

1064 **References**

1065 Abimbola, D.A. (2016). A Re-evaluation of the Depositional Environments and Sedimentary
1066 Facies of Middle Miocene Paralic Deposits (Agbada Formation), Ewan and Oloye Fields,
1067 Northwestern Niger Delta. *Journal of Marine Science: Research & Development*.

1068

1069 Agard, P., Omrani, J., Jolivet, L., Whitechurch, H., Vrielynck, B., Spakman, W., Monie, P.,
1070 Meyer, B., & Wortel, R. (2011). Zagros orogeny: A subduction-dominated process. *Geol. Mag*,
1071 148 (5–6), 689–691.

1072

1073 Allmendinger, R.W., Jordan, T.E., Kay, S.M., & Isacks, B.L. (1997). The evolution of the
1074 Altiplano-Puna Plateau of the central Andes. *Journal of Annual Review of Earth and Planetary
1075 Sciences*, 25, 139–174.

1076

1077 Alvarado, P., Beck, S., & Zandt, G. (2007). Crustal structure of the south-central Andes
1078 Cordillera and backarc region from regional waveform modelling. *Journal of Geophys. J. Int.*,
1079 170, 858–875, doi: 10.1111/j.1365-246X.2007.03452.x.

1080

1081 Alonso, B., E Field, M., V Gardner, J., & Maldoando, A. (1990). Sedimentary evolution of the
1082 Pliocene and Pleistocene Ebro margin. northeastern Spain. *Marine Geology*, 95, 313-331.

1083

1084 Amini, B. (1969). Geological map of Tarom. Geological Survey of Iran, Tehran, scale 1:100,000

1085

1086 Maggi, A., Jackson, J.A., McKenzie, D. & Priestley, K. (2000). Earth-quake focal depths,
1087 effective elastic thickness, and the strength of the continental lithosphere. *Geology*, 28. 459–498

1088

1089 Ballato, P., Brune, S., & Strecker, M.R. (2019). Sedimentary loading–unloading cycles and
1090 faulting in intermontane basins: Insights from numerical modelling and field observations in the
1091 NW Argentine Andes. *Earth and Planetary Science Letters*, 506, 388-396.

1092

1093 Ballato, P., Cifelli, F., Heidarzadeh, G.H., Ghassemi, M.R., Wicert, A.D., Hassanzadeh, J.,
1094 Dupont–nivet, G., Balling, P., Sudo, M., Zeiliger, G., Schmit, A.K., Mattei, M., & Strecker, M.R.
1095 (2017). Tectono-sedimentary evolution of the northern Iranian Plateau: insights from middle-late
1096 Miocene foreland-basin deposits. *Basin Research*, 29, 1–30.

1097

1098 Ballato, P., Landgraf, A., Fox, M., Stockli, D., Schildgen, T.F., Ghassemi, M.R., Kirby, E., &
1099 Strecker, M.R. (2015). The growth of a mountain belt forced by base-level fall: tectonics and
1100 surface processes during the evolution of the Alborz Mountains, N Iran. *Earth Planet. Sci. Lett.*,
1101 425, 204–218.

1102

- 1103 Ballato, P., Nowaczy, N.R., Landgraf, A., Strecker, M.R., Friedrich, A., & Tabaei, S.H. (2008).
1104 Tectonic control on sedimentary facies pattern and sediment accumulation rates in the Miocene
1105 foreland basin of the southern Alborz Mountains, northern Iran. *Tectonics*, 27, TC6001.
1106
- 1107 Ballato, P., Stockli, D.F., Ghassemi, M.R., Landgraf F, A., Strecker, M.R., Hassanzadeh, J.,
1108 Friedrich, A., & Tabatabei, S.H. (2013). Accommodation of transpressional strain in the Arabia-
1109 Eurasia collision zone: new constraints from (UTh)/He thermochronology in the Alborz
1110 Mountains, N Iran. *Tectonics*, 32, 1–18.
1111
- 1112 Ballato, P., Uba, C.E., Landgraf, A., Strecker, M.R., Sudo, M., Stockl, D.F., Friedrich, & A.,
1113 Tabatabei, S. H. (2011). Arabia-Eurasia continental collision: Insights from late Tertiary
1114 foreland-basin evolution in the Alborz Mountains, northern Iran. *Geological Society of America*
1115 *Bulletin*, 123, 106–131.
1116
- 1117 Barber, D.E., Stockli, D.F., Horton, B.K., & Koshnaw, R.I. (2018). Cenozoic Exhumation and
1118 Foreland Basin Evolution of the Zagros Orogen During the Arabia-Eurasia Collision, Western
1119 Iran. *Tectonics*, 37, 4396–4420. <https://doi.org/10.1029/2018TC005328>.
1120
- 1121 Berberain, M., & Walker, R. (2010). The Rudbār Mw 7.3 earthquake of 1990 June 20;
1122 seismotectonics, coseismic and geomorphic displacements, and historic earthquakes of the
1123 western ‘High-Alborz’, Iran. *Geophysical Journal International*, 182, 1577–1602.
1124
- 1125 Blair, T.C. (1999). Sedimentology of the debris-flow-dominated Warm Spring Canyon alluvial
1126 fan, Death Valley, California. *Sedimentology*, 46, 941–965.

1127

1128 Boothroyd, J.C., & Ashley, G.M. (1975). Processes, bar morphology, and sedimentary
 1129 structures on braided outwash fans, Northeastern Gulf of Alaska. *The Society of Economic*
 1130 *Paleontologists and Mineralogist (SEPM); Glaciofluvial and Glaciolacustrine Sedimentation*
 1131 (SP23).

1132

1133 Borradaile, G.J., & Henry, B. (1997). Tectonic applications of magnetic susceptibility and its
 1134 anisotropy. *Earth Sci Rev*, 42, 49–93.

1135

1136 Borradaile, G. J. (1988). Magnetic susceptibility, petrofabrics and strain. *Tectonophysics*, 156, 1-
 1137 20.

1138

1139 Borradaile, G. J. (2001). Magnetic fabrics and petrofabrics: Their orientation distribution and
 1140 anisotropies. *J. Struct. Geol*, 23, 1581–1596.

1141

1142 Brunet, M., Korotaev, M.V., Ershov, A.V., & Nikishin, A.M. (2003). The South Caspian Basin:
 1143 a review of its evolution from subsidence modelling. *Sedimentary Geology*, 156, 119-148.

1144

1145 Carroll, A.R., Graham, S.A., & Smith, M.E. (2010). Tectonic and Stratigraphic Evolution of
 1146 Nonmarine Basins of China. *Basin Research*, 22, 17 - 32.

1147

1148 Castellanos, D.G. (2007). The role of climate during high plateau formation Insights from
 1149 numerical experiments. *Earth and Planetary Science Letters*, 257, 372–390.

1150

1151 Charreauh, J., Chen, Y., Gilder, S., Dominguez, S., Avouac, J.PH. Sen, S., Sun, D., Li, Y., &
1152 Wang, W.M. (2005). Magnetostratigraphy and rock magnetism of the Neogene Kuitun He
1153 section (northwest China): Implications for Late Cenozoic uplift of the Tianshan mountains.
1154 *Earth and Planetary Science Letters*, 230, 177–192.

1155

1156 Chiu, H.-Y., Chung, S.-L., Zarrinkoub, M.H., Mohammadi, S.S., Khatib, M.M., & Iizuka, Y.
1157 (2013). Zircon U–Pb age constraints from Iran on the magmatic evolution related to Neotethyan
1158 subduction and Zagros orogeny. *Lithos*, 162–163, 70–87.

1159

1160 Cifelli, F., Ballato, P., Alimohammadian, H., Sabouri, J., & Mattei, M. (2015). Tectonic
1161 magnetic lineation and oroclinal bending of the Alborz range: Implications on the Iran-Southern
1162 Caspian geodynamics. *Tectonic*, 234, 116-132.

1163

1164 Davies, R.G. (1977). Geological map of Bandar e Pahlavi quadrangle. Geological Survey of Iran,
1165 Tehran, scale 1:250,000.

1166

1167 Davies, D., Suppe, J., & Dahlen, F.A. (1983). Mechanics of fold-and-thrust belts and
1168 accretionary wedges. *J. Geophys. Res*, 88, 1153–72.

1169

1170 Davoudzadeh, M., Lammerer, B., & Weber-Diefenbach, K. (1997). Paleogeography,
1171 Stratigraphy, and Tectonics of the Tertiary of Iran. *Neues Jahrbuch für Geologie und*
1172 *Paläontologie – Abhandlungen*, 205, 33-67.

1173

1174 Dewey, J.F., & Burke, K. (1974). Hot spots and continental break-up: implications for collisional
1175 orogeny. *Geology*, 2, 57–60.

1176

1177 Dewey, J.F. (1988). Extensional collapse of orogens. *Tectonics*, 7, 1123–1139.

1178

1179 Dickinson, W.R. (1985). Interpreting provenance relations from detrital modes of sandstones. In:
1180 Zuffa, G.G. (Ed.), *Provenance of arenites*. Reidel, Dordrecht, NATO ASI Series, 148, 333–361.

1181 Djamour, Y., Vernant, P.H., Bayer, R., Nankali, H.R., Ritz, J.F., Hinderer, J., Hatam, Y., Luck,
1182 B., & Moigne, N.L. (2010). GPS and gravity constraints on continental deformation in the
1183 Alborz Mountain range, Iran. *Geophysical Journal International*, 183, 1287-1301.

1184

1185 Dupont-Nivet, G., & Krijgsman, W. (2012). Magnetostratigraphic methods and applications, in
1186 Busby, C., Azor, A. (eds.), *Recent Advances in Tectonics of Sedimentary Basins*, Wiley-
1187 Blackwell, p 80-94.

1188

1189 Ejiuba, C., Heubeck, C., & Hulka, C. (2005). Facies analysis and basin architecture of the
1190 Neogene Subandean synorogenic wedge, southern Bolivia. *Sedimentary Geology*, 180, 91–123.

1191 Engdahl, E., Jackson, J., Myers, S., Bergman, E., & Priestley, K. (2006). Relocation and
1192 assessment of seismicity in the Iran region. *Geophys. J. Int.*, 167, 761–788.

1193

1194 England, P.H., & McKenzie, D. (1982). A thin viscous sheet model for continental deformation.
1195 *Geophysical Journal of the Royal Astronomical Society*, 170, 295–32.

1196

1197 Francois, T., Agard, P., Bernet, M., Meyer, B., Chung, S.L., Zarrinkoub, M.H., Burov, E. &
1198 Moni_E, P. (2014). Cenozoic exhumation of the internal Zagros: first constraints from low-
1199 temperature thermochronology and implications for the build-up of the Iranian plateau. *Lithos*,
1200 206–207, 100–112.

1201

1202 Faccenna, C., Becker, T.W., Jolivet, L. & Keskin, M. (2013). Mantle convection in the Middle
1203 East: reconciling Afar upwelling, Arabia indentation and Aegean trench rollback. *Earth Planet.*
1204 *Sci. Lett.*, 373, 254–269.

1205

1206 François, T., Burov, E., Agard, P., & Meyer, B. (2014). Buildup of a dynamically supported
1207 orogenic plateau: Numerical modeling of the Zagros/Central Iran case study, *Geochem.*
1208 *Geophys. Geosyst.*, 15, 2632–2654, doi:10.1002/2013GC005223.

1209

1210 Forte, A.M., & Cowhill, E. (2013). Late Cenozoic base-level variations of the Caspian Sea: a
1211 review of its history and proposed driving mechanisms. *Palaeogeogr. Palaeo-climatol.*
1212 *Palaeoecol.*, 386, 392–407.

1213

1214 Francois, T., Burov, E., Agard, P., & Meyer, B. (2014). Buildup of a dynamically supported
1215 orogenic plateau: Numerical modeling of the Zagros/Central Iran case study; *Geochem.*
1216 *Geophys. Geosyst.*, 15, 2632–2654.

1217

1218 Garzanti, E.D. (2019). Petrographic classification of sand and sandstone. *Earth-Science Reviews*,
1219 192, 545–563.

1220

1221 Chang, H., An, ZH., Liu, W., Qiang, X., Song, Y., & Ao, H. (2012). Magnetostratigraphic and
1222 paleoenvironmental records for a Late Cenozoic sedimentary sequence drilled from Lop Nor in
1223 the eastern Tarim Basin, *Global and Planetary Change*, 80–81, 113–122.

1224 Ghinass, M., D’oriano, F., Benvenuti, M., Fedi, M., & Awramik., S. (2015). Lacustrine Facies in
1225 Response to Millennial-Century-Scale Climate Changes (Lake Hayk, Northern Ethiopia), *Journal*
1226 *of Sedimentary Research*, 85, 381–398.

1227 Chakraborty, T., & Soumendar, S. (2005). Evidence of lacustrine sedimentation in the Upper
1228 Permian Bijori Formation, Satpura Gondwana basin, Palaeogeographic and tectonic implications,
1229 *Journal of Earth System Science*, 114, 303–323.

1230

1231 Ghibaudo, G.U. (1992). Subaqueous sediment gravity flow deposits: practical criteria for their
1232 field description and classification. *Sedimentology (IAS)*, 39, 423-454.

1233

1234 Gradstein, F.M., Ogg, J.G., Schmitz, M., & Ogg, G. (2012). *The Geologic Time Scale 2012*.
1235 Elsevier, Cambridge University Press, Cambridge.

1236

1237 Guest, B., Axen, G.J., Lam, P.S., & Hassanzadeh, J. (2006a). Late Cenozoic shortening in the
1238 west central Alborz Mountains, northern Iran, by combined conjugate strike-slip and thin-
1239 skinned deformation. *Geosphere*, 2, 35–52.

1240

1241 Guest, B., Horton, B.K., Axen, G.J., Hassanzadeh, J., & McIntosh, W.C. (2007). Middle to late
1242 Cenozoic basin evolution in the western Alborz Mountains: Implications for the onset of
1243 collisional deformation in northern Iran. *Tectonics*, 26, TC6011.

1244

1245 Guest, B., Stockli, D. F., Grove, M., Axen, G. J., Lam, P. S., & Hassanzadeh, J. (2006b).
1246 Thermal histories from the central Alborz Mountains, northern Iran: Implications for the spatial
1247 and temporal distribution of deformation in northern Iran. *Geological Society of America*
1248 *Bulletin*, 118, 1507-1521.

1249

1250 Hassanzadeh, J., Stockli, D. F., Horton, B. K., Axen, G. J., Stockl, L. D., & Grove, M. (2008). U-
1251 Pb zircon geochronology of late Neoproterozoic- Early Cambrian granitoids in Iran: Implications
1252 for paleogeography, magmatism, and exhumation history of Iranian. 778 basement.
1253 *Tectonophysics*, 451, 71–96.

1254

1255 Hatzfeld, D., & Molnar, P. (2010). Comparisons of the kinematics and deep structures of the
1256 Zagros and Himalaya and of the Iranian and Tibetan plateaus and geodynamic implications, *Rev.*
1257 *Geophys*, 48, 2.

1258

1259 Heidarzadeh, G.H., Ballato, P., Hassanzadeh, J., Ghassemi, M.R., & Strecker, M.R. (2017). Lake
1260 Overspill and onset of fluvial incision in the Iranian Plateau: insights from the Mianeh Basin;
1261 *Planetary Science Letters* 469, 135-147.

1262

1263 Hein, F.J. (1982). Depositional mechanisms of deep-sea coarse clastic sediments, Cap Enrage
1264 Formation, Quebec. *Canadian Journal Earth Science*, 19, 267–287.

1265
1266 Hermanns, R.L., & Strecker, M.R. (1999). Structural and lithological controls on large
1267 Quaternary rock avalanches (sturzstroms) in arid northwestern Argentina. *Geological Society of
1268 America Bulletin*, 111, 934-948.

1269
1270 Hilley, G.E, Strecker, M.R., & Ramos, V.A. (2004). Growth and erosion of fold-and-thrust belts
1271 with an application to the Aconcagua fold-and-thrust belt, Argentina. *J. Geophys. Res*, 109, B1.

1272
1273 Hilley, G.E., & Strecker, M.R. (2004). Steady state erosion of critical Coulomb wedges with
1274 applications to Taiwan and the Himalaya. *J. Geophys. Res*, 109, B1.

1275
1276 Horton, B.K., Hassanzadeh, J., Stockli, D.F., Axen, G.J., Gillis, R.J., Guest, B., Amini, A.,
1277 Fakhari, M.D., Zamanzadeh, S.M., & Grove, M. (2008). Detrital zircon provenance of
1278 Neoproterozoic to Cenozoic deposits in Iran: Implications for chronostratigraphy and collisional
1279 tectonics: *Tectonophysics*, 451, 97–122.

1280
1281 Horton, B.K. (2018). Tectonic regimes of the Central and Southern Andes: responses to
1282 variations in plate coupling during subduction. *Tectonics*, 37 (2), 402–429.

1283
1284 Horton, K.B., & Schmitt, J.G. (1996). Sedimentology of a lacustrine fan-delta system, Miocene
1285 Horse Camp Formation, Nevada, USA. *Sedimentology*, 43, 133–155.

1286

- 1287 Horton, B. K. (2012). Cenozoic evolution of Hinterland Basins in the Andes and Tibet. In C.
 1288 Busby, & A. Azor (Eds.), *Tectonics of Sedimentary Basins: Recent advances* (pp. 427–444).
 1289 New York, NY: John Wiley & Sons, Ltd.
 1290
- 1291 Hrouda, F. (1982). Magnetic anisotropy of rocks and its application in geology and geophysics.
 1292 *Suveys in Geophysics*, 5, 37–82.
 1293
- 1294 Huang, B., Piper, J.D.A., Peng, SH., Liu, T., LI, ZH., Wang, Q., & Zhu, R. (2006).
 1295 Magnetostratigraphic study of the Kuche Depression, Tarim Basin, and Cenozoic uplift of the
 1296 Tian Shan Range, Western China, *Earth and Planetary Science Letters*, 251, 346–364.
 1297
- 1298 Ilgar, A., & Nemeç, W. (2005). Early Miocene lacustrine deposits and sequence stratigraphy of
 1299 the Ermenek Basin, Central Taurides, Turkey, *Sedimentary Geology*, 173, 233-275.
 1300
- 1301 Ingersoll, R.V., Bullaëd, T.F., Ford, R.L., Grimm, J.P., Pickle, J.D., & Sares, S.W. (1984). the
 1302 effect of grain size on detrital modes: a test of the Gazzi–Dickinson point-counting method.
 1303 *Journal of Sedimentary Petrology*, 54, 103 –116.
 1304
- 1305 Isacks, B.L. (1988). Uplift of the central Andean Plateau and bending of the Bolivian Orocline, *J.*
 1306 *Geophys. Res* 93, 3211–3231.
 1307
- 1308 Jimenez-Munt, I., Fernandez, M., Saura, E., Verges, J., & Garcia-Castellanos, D. (2012). 3-D
 1309 lithospheric structure and regional/residual Bouger anomalies in the Arabia-Eurasia collision
 1310 (Iran). *Geophys. J. Int* 190, 1311–1324.

- 1311
- 1312 Jordan, T.E. & Allmendinger, R.W. (1986). The Sierras Pampeanas of Argentina: a modern
1313 analogue of Rocky Mountain foreland deformation. *Am. J. Sci.*, 286, 737–764.
- 1314
- 1315 Keighley, D. (2008). A lacustrine shoreface succession in the Albert Formation, Moncton Basin,
1316 New Brunswick, *Bulletin of Canadian Petroleum Geology*, 56, 235-258.
- 1317 Kley, J., & Monaldi, C.R. (2002). Tectonic inversion in the Santa Barbara system of the central
1318 Andean foreland thrust belt, northwestern Argentina: *Tectonics*, v. 21, p. 1–18, 1061.
- 1319
- 1320 Kodama, K.P. (2012). *Paleomagnetism of Sedimentary Rocks: Process and Interpretation*
1321 *Science*, p 184.
- 1322
- 1323 Koshnaw, R.I., & Stockli, D.F. (2018). Timing of the Arabia-Eurasia continental collision-
1324 Evidence from detrital zircon U-Pb geochronology of the Red Bed Series strata of the northwest
1325 Zagros hinterland, Kurdistan region of Iraq. *Geology*, 47, 47-50.
- 1326
- 1327 Kraus, M.J. (1999). Paleosols in clastic sedimentary rocks: their geologic applications. *Earth*
1328 *Science Reviews*, 47, 41-70.
- 1329
- 1330 Lamb, S., Hoke, L., Kennan, L., & Dewey, J. (1997). Cenozoic Evolution of the Central Andes
1331 in Bolivia and Northern Chile, ed. JP Burg, M Ford, 121, 237–64.
- 1332
- 1333 Langereis, C.G, Krijgsman, W., Muttoni, G., & Menningning, M. (2010). Magnetostratigraphy;
1334 concepts, definitions, and applications. *Newsletter on Stratigraphy*, 43/3, 207–233.

- 1335
- 1336 Larrasoana, J.C., Pueyo, E.L., & Pares, J.M. (2004). An integrated AMS, structural, palaeo- and
1337 rock-magnetic study of Eocene marine marls from the Jaca-Pamplona basin (Pyrenees, N Spain);
1338 new insights into the timing of magnetic fabric acquisition in weakly deformed mudrocks.
1339 Geological Society, London, Special Publications, 238 (1), 127.
- 1340
- 1341 Lowenstein, T.K., & Hardie, L.A. (1985). Criteria for the recognition of salt-pan evaporites.
1342 *Sedimentology*, 32, 627–644.
- 1343 Madanippur, S., Ehlres, T., Yassaghi, A., Rezaeian, M., Enkelmann, E., & Bahroudi, A. (2013).
1344 Synchronous deformation on orogenic plateau margins: insights from the Arabia-Eurasia
1345 collision. *Tectonophysics*, 608, 440–451.
- 1346
- 1347 Madanippur, S., Ehlres, T.A., Yassaghi, A., & Enkelmann, E. (2017). Accelerated middle
1348 Miocene exhumation of the Talesh Mountains constrained by U-Th/He thermochronometry:
1349 Evidence for the Arabia-Eurasia collision in the NW Iranian Plateau. *Tectonics*, 36, 1538-1561.
- 1350
- 1351 Madanippur, S., Yassaghi, A., Todd Ehlers, T.A., & Enkelmann, E. (2018).
1352 Tectonostratigraphy, structural, geometry and kinematics of the NW Iranian Plateau margin:
1353 Insight from the Talesh Mountains, Iran. *American Journal of Science*, 318, 208-245.
- 1354
- 1355 Maizels, J. (1989). Sedimentology, paleoflow dynamics and flood history of jokulhlaup deposits;
1356 paleohydrology of Holocene sediment sequences in southern Iceland sandur deposits. *Journal of*
1357 *Sedimentary Research*, 59, 204-223.

- 1358
- 1359 Mattei, M., Cifelli, F., Muttoni, G., & Rashid, H. (2015). Post-Cimmerian (Jurassic–Cenozoic)
- 1360 paleogeography and vertical axis tectonic rotations of Central Iran and the Alborz Mountains. *J.*
- 1361 *Asian Earth Sci*, 102, 92–101.
- 1362 Mattei, M., Cifelli, F., Alimohammaadian, H., Rashid, H., Winkert, A., & Sagnotti, L. (2017).
- 1363 Oroclinal bending in the Alborz Mountains (Northern Iran): New constraints on the age of South
- 1364 Caspian subduction and extrusion tectonics, *Gondwana Research*, 42, 13-28.
- 1365
- 1366 Mattei, M., Visconti, L. A., Cifelli, F., Nozaem, R., Winkert, A., & Sagnotti, L. (2019).
- 1367 Clockwise paleomagnetic rotations in north-eastern Iran: Major implications on recent
- 1368 geodynamic evolution of outer sectors of the Arabia-Eurasia collision zone, *Gondwana*
- 1369 *Research*, 71, 194-209.
- 1370
- 1371 Mattei, M., Cifelli, F., Alimohammaadian, H., & Rashid, H. (2020). The role of active strike-slip
- 1372 faults and opposite vertical axis rotations in accommodating Eurasia-Arabia shortening in
- 1373 Central Iran. *Tectonophysics*, 774, 228-243.
- 1374 Mcfadden, P.L., & Mcelhinny, M.W. (1990). Classification of the reversal test in
- 1375 palaeomagnetism. *Geophys. J. Int*, 103, 725–729.
- 1376
- 1377 Meyer, B., Tappnnier, P., Bourjot, L., Me´tiver, F., Gaudemer, Y., Peltzer, G., Guo, S., & Chen,
- 1378 Z. (1998). Crustal thickening in Gansu-Qinghai, lithospheric mantle subduction, and oblique,
- 1379 strike-slip controlled growth of the Tibet Plateau. *Geophys. J. Int*, 135, 1– 47.
- 1380

- 1381 Miall, A.D. (1978). Lithofacies types and vertical profile models in braided river deposits.
1382 Fluvial Sedimentology: Canadian Society Petrology Geology Memoir, 5, 597–604.
1383
- 1384 Miall, A.D. (1985). Architectural-Element Analysis: A New Method of Facies Analysis Applied
1385 to Fluvial Deposits. Earth-Science Reviews, 22, 261-308.
1386
- 1387 Miall, A.D. (1996). The Geology of Fluvial Deposits. Springer Verlag, Berlin XVI, 582 pp.
1388
- 1389 Miall, A.D. (1997). A review of the braided river depositional environment. Earth Science
1390 Review, 13, 1–62.
1391
- 1392 Monlar, P., England, P.H., & Martiod, J. (1993). Mantle dynamics, uplift of the Tibetan Plateau,
1393 and the Indian Monsoon. Reviews of Geophysics, 31, 357-396.
1394
- 1395 Motaghi, K., Ghods, A., Sobouti, F., Shabanian, E., Mahmoudabadi, M., & Priestly, K. (2018).
1396 Lithospheric seismic structure of the West Alborz – Talesh ranges, Iran. Geophysical Journal
1397 International, 215, 1766-1780.
1398
- 1399 Morley, C., Kongwung, B., Julapour, A.A., Abdolghafourian, A., Hajian, M., Waples, D.,
1400 Warren, J., Otterdoom, H., Srisuriyon, K., & Kazemi, H. (2009). Structural development of the
1401 major Late Cenozoic basin and transpressional belt in Central Iran: the Central Basin in the
1402 Qom-Saveh area. Geosphere, 5, 325–362.
1403

1404 Mouthereau, F., Lacombe, O., & Verges, J. (2012). Building the Zagros collisional orogen:
1405 timing, strain distribution and the dynamics of Arabia/Eurasia plate convergence.
1406 *Tectonophysics*, 532-535, 27-60.

1407

1408 Mouthereau, F., Lacombe, O., & Verges, J. (2012). Building the Zagros collisional orogen:
1409 timing, strain distribution and the dynamics of Arabia/Eurasia plate convergence.
1410 *Tectonophysics*, 532-535, 27-60.

1411

1412 Nabatian, GH. Ghaderi, M., Neubauer, F., Honaemand, M., Liu, X., Dong, Y., Jjang, S.H.Y.,
1413 Quadt, A.V., & Bernroider, M. (2014). Petrogenesis of Tarom high-potassic granitoids in the
1414 Alborz-Azarbaijan belt, Iran: Geochemical, U-Pb zircon and Sr-Nd-Pb isotopic constraints.
1415 *Lithos*, 184-187, 324-345.

1416

1417 Omrani, H., Moazzen, M., Oberhansli, R., Tsujimori, T., Bousquet, R., & Moayyed, M. (2013).
1418 Metamorphic history of glaucophane-paragonite-zoisite eclogites from the Shanderman area,
1419 northern Iran. *Journal of Metamorphic Geology*, 31, 791-812.

1420

1421 Paknia, M., Ballato, P., & Mattei, M. (2019). An integrated paleomagnetic, rock magnetic,
1422 anisotropy of magnetic susceptibility, stratigraphic and structural study of Miocene synorogenic
1423 red beds from NW Iran: Insight into the geologic evolution of the intermontane Tarom Basin at
1424 the linkage between the western Alborz Mountains and the northern margin of the Iranian
1425 Plateau.

1426 PhD thesis; chapter III, Department of Science, Unievrnsity of Roma Tre, Ciclo Del Corso Di
1427 Dottorato XXXII.

1428
1429 Pares, J.M. (2004). How deformed are weakly deformed mudrocks? Insights from magnetic
1430 magnetic anisotropy. In: Martin-Hernandez, F., Lüneburg, C., Aubourg, C., Jackson, M. (Eds.),
1431 Magnetic Fabrics: Methods and Applications. Geological Society, London, Special Publication,
1432 238, 191–203.

1433
1434 Pingel, H., Alonso, R.N., Altenberger, U., Cottle J., & Strecker, M.R. (2019). Miocene to
1435 Quaternary basin evolution at the southeastern Andean Plateau (Puna) margin ca. 24°S lat,
1436 Northwestern Argentina. *Basin Research*, 32, 808-826.

1437
1438 Pingel, H., Schildgen, T., & Strecker, M.R. (2019). Hella Wittmann, Pliocene–Pleistocene
1439 orographic control on denudation in northwest Argentina. *Geology*, 47, 359-362.

1440
1441 Pirouzouz, M., Avouzc, J-P., Hassanzadeh, J., Kirschvink, J.L., & Bahroudi, A. (2017). Early
1442 Neogene foreland of the Zagros, implications for the initial closure of the Neo-Tethys and
1443 kinematics of crustal shortening. *Earth and Planetary Science Letters*, 477, 168–182.

1444
1445 Puy-Aquiza, M.J., Mirand-Aviles, R., Garcia-Barragan, J.C., Loza-Aguirre, I., Li, Y., &
1446 Anazanor, G. (2017). Facies analysis, stratigraphic architecture and depositional environments of
1447 the Guanajuato conglomerate in the Sierra de Guanajuato, Mexico. *Boletín de la Sociedad*
1448 *Geológica Mexicana*, 69, 385-408.

1449

1450 R. Merrill, R., Mcfadden, P., & Mcelhinny, M. (1996). The Magnetic Field of the Earth:
 1451 Paleomagnetism, the Core, and the Deep Mantle. International geophysics series ISSN 0074-
 1452 6142; Academic Press, San Diego, p 531.

1453

1454 Rabiee, A., Rossetti, F., Asahara, Y., Azizi, H., Glodny, J., Lucci, F., Lustrino, M., Nozaem, R.
 1455 (2020). Long-lived, Eocene-Miocene stationary magmatism in NW Iran along a transform plate
 1456 boundary, NW Iran, Gondwana Research.

1457

1458 Rahmani, M., Motaghi, K., Ghods, A., Sobouti, F., Talebian, M., Ai, Y., & Chen, L. (2019).
 1459 Deep velocity image of the north Zagros collision zone (Iran) from regional and teleseismic
 1460 tomography. *Geophys. J. Int.* 219, 1729–1740.

1461

1462 Reiners, P.W., & Brandon, M.T. (2006). Using thermochronology to understand orogenic
 1463 erosion. *Annu. Rev. Earth Planet. Sci*, 34, 419–66.

1464

1465 Reuter, M., Piller, W. E., Harzhauser, M., Mandic, O., Berning, B., & Rogl, F. (2009). The
 1466 Oligo-/Miocene Qom Formation (Iran): Evidence for an early Burdigalian restriction of the
 1467 Tethyan Seaway and closure of its Iranian gateways. *International Journal of Earth Sciences*, 98,
 1468 627–650.

1469

1470 Rezaeian, M., Carter, A., Hovius, N., & Allen, M.B. (2012). Cenozoic exhumation history of the
 1471 Alborz Mountains, Iran: New cconstraints from low-temperature chronometry. *Tectonics*, 31,
 1472 TC2004.

1473

1474 Richardson, T., Gilbert, H., Anderson, M., & Ridgway, K.D. (2012). Seismicity within the
1475 actively deforming eastern Sierras Pampeanas, Argentina. *Geophys. J. Int.* 188, 408e420.

1476

1477 Ridgway, K.D., & Decelles, P.G. (1993). Stream-dominated alluvial fan and lacustrine
1478 depositional systems in Cenozoic strike-slip basins, Denali fault system, Yukon Territory,
1479 Canada. *Sedimentology*, 140, 645-666.

1480

1481 Rieben, H. (1955). The geology of the Tehran plain. *American Journal of Science* 253, 617–639.

1482 Robert, A.M.M., Letouzey, J., Kavooosi, M.A., Sherkati, S.H., Muller, C., (2014). Structural
1483 evolution of the Kopeh Dagh fold-and-thrust belt (NE Iran) and interactions with the South
1484 Caspian Sea Basin and Amu Darya Basin. *Marine and Petroleum Geology*, Elsevier, 57, 68-87.

1485

1486 Robion, P., Grelaud, S., & Frizon de lamotte, D. (2007). Pre-folding magnetic fabrics in fold
1487 and-thrust belts: Why the apparent internal deformation of the sedimentary rocks from the
1488 Minervois basin (NE-Pyrenees, France) is so high compared to the Potwar basin (SW-Himalaya,
1489 Pakistan)? *Sediment. Geol.* 196, 181–200.

1490

1491 Royden, L. (1996). Coupling and decoupling of crust and mantle in convergent orogens:
1492 Implications for strain partitioning in the crust, *J. Geophys. Res.* 101, 17, 679–17, 705.

1493

1494 Royde, L.H., Burchfiel, B. C., King, R.W., Wang, E., Chen, Z., Shen, F., & Liu, Y. (1997).
1495 Surface deformation and lower crustal flow in Eastern Tibet. *Science*, 276 (5313), 788–790.

1496

1497 R.X., Potts, R., Pan, Y.X., Lu, L.Q., Yao, H.T., Deng, C.L., & Qin, H.F. (2008). Paleomagnetism
1498 of the Yuanmou Basin near the southeastern margin of the Tibetan Plateau and its constraints on
1499 late Neogene sedimentation and tectonic rotation, *Earth and Planetary Science Letters*, 272, 97–
1500 104.

1501
1502 Saint-Bezar, B., Hebert, R.L., Aubourg, C., Robion, P., Swenen, R. Frizon de, & Lamotte, D.
1503 (2002). Magnetic fabric and petrographic investigations of hematite-bearing sandstones within
1504 ramp-related folds: examples from the South Atlas Front (Morocco). *J. Struct. Geol*, 24, 1507–
1505 1520.

1506
1507 Schildgen, T., Robinson, R.A.J., Savi, S., Phillips, W.M., Spencer, J.Q.G., Bookhagen, B.,
1508 Scherler, D., Tofelde, S., Alonso, R.N., Kunik, P.W., Binnie, S.A., & Strecker, M.R. (2016).
1509 Landscape response to late Pleistocene climate change in NW Argentina: sediment flux
1510 modulated by basin geometry and connectivity. *J. Geo-phys. Res*, 121, 392–414.

1511
1512 Siks, B.C., & Horton, B.K. (2011). Growth and fragmentation of the Andean foreland basin
1513 during eastward advance of fold-thrust deformation, Puna plateau and Eastern Cordillera,
1514 northern Argentina. *Tectonic*, 30.

1515
1516 Sobel, E.R., & Strecker, M.R. (2003). Uplift, exhumation and precipitation: Tectonic and
1517 climatic control of late Cenozoic landscape evolution in the northern Sierras Pampeanas,
1518 Argentina. *Basin Research*, 15, 431–451.

1519

1520 Sobel, E.R., Hilley, G.E., & Strecker, M.R. (2003). Formation of internally drained contractional
1521 basins by aridity-limited bedrock incision. *J. Geophys. Res. Solid Earth*, 108, JB001883.

1522

1523 Soto, R., Larrasoana, J.C., Arlegui, L.E., Beamud, E., Olivaurcia, B., & Simon, J.L. (2009).
1524 Reliability of magnetic fabric of weakly deformed mudrocks as a palaeostress indicator in
1525 compressive settings. *J. Struct. Geol.*, 31, 512–522.

1526

1527 Stanistreet, I.G., & McCarthy, T.S. (1993). The Okavango Fan and the classification of subaerial
1528 fan systems. *Sedimentary Geology*, 85, 115–133.

1529

1530 Stocklin, J., & Eftekharneshad, J. (1969). Geological map of Zanjan quadrangle. Geological
1531 Survey of Iran, Tehran scale 1:250,000.

1532 Strecker, M.R., Alonso, R., Bookhagen, B., Carrpapa, B., Coutand, I., Hain, M.P., Hilley, G.E.,
1533 Mortimer, E., Schoenbohm, L., & Sobel, E.R. (2009). Does the topographic distribution of the
1534 central Andean Puna Plateau result from climatic or geodynamic processes. *Geology*, 37, 643–
1535 646.

1536

1537 Strecker, M. R., Hilley, G. E., Bookhagen, B., & Sobel, E. R. (2012). Structural, geomorphic,
1538 and depositional characteristics of contiguous and broken foreland basins: Examples from the
1539 eastern flanks of the central Andes in Bolivia and NW Argentina, in *Tectonics of Sedimentary*
1540 *Basins: Recent Advances*, edited by C. Busby and A. Azor, pp. 508–521, John Wiley,
1541 Chichester, UK. doi: 10.1002/9781444347166.ch25

1542

- 1543 Strecker, M.R., Alonso, R.N., Bookhagen, B., Carrapa, B., Hilley, G.E., Sobel, E.R., & Truth,
 1544 M.H. (2007). Tectonics and Climate of the Southern Central Andes. *Annu. Rev. Earth Planet*, 35,
 1545 747-787.
- 1546
- 1547 Streit, R.L., Burbank, D.W., Strecker, M.R., Alonso, R.N., Cottle, J.M., & Kulander-Clark,
 1548 A.R.C. (2015). Controls on intermontane basin filling, isolation and incision on the margin of the
 1549 Puna plateau, NW Argentina (~23°S). *Basin Research*, 29, 131–155.
- 1550
- 1551 Tadayon, M., Rosseti, F., Zattin, M., Calzolari, G., Nozaem, R., Salvini, F., Cladio, F., &
 1552 Khoabakhshi, P. (2018). The long-term evolution of the Doruneh Fault region (Central Iran): A
 1553 key to understanding the spatio-temporal tectonic evolution in the hinterland of the Zagros
 1554 convergence zone. *Geological journal*, 54, 1454-1479.
- 1555
- 1556 Tarling, D. H., & Hrouda, F. (1993). *The Magnetic Anisotropy of Rocks*. London: Chapman &
 1557 Hall, 217 p.
- 1558
- 1559 Tha, H.V, Wysocka, A., Pha, P.D., Cuong, N.Q., & Ziolkowski, P. (2015). Lithofacies and
 1560 depositional environments of the Paleogene/Neogene sediments in the Hoanh Bo Basin (Quang
 1561 Ninh province, NE Vietnam). *Geology, Geophysics & Environment*, 41, 353–369.
- 1562
- 1563 Thiede, R., Bookhagen, B., Arrowsmith, J.R, Sobel, E., & Strecker, M.R. (2004). Climatic
 1564 control on rapid exhumation along the southern Himalayan front. *Earth Planet. Sci. Lett*, 222,
 1565 791–806.

1566

1567 Todd, S.P. (1989). Stream-driven, high-density gravelly traction carpets: possible deposits in the
1568 Trabeg Conglomerate Formation, SW Ireland and some theoretical considerations of their origin.
1569 *Sedimentology (IAS)*, 36, 513-735.

1570

1571 Tofelde, S., Schildgen, T.F., Savi, S., Pingel, H., Wickert, A.D., Bookhangen, B., Wittmann, H.,
1572 Alonso, R.N., Cottle, J., & Strecker, M.R. (2017). 100kyr fluvial cut-and-fill terrace cycles since
1573 the Middle Pleistocene in the southern Central Andes, NW Argentina. *Earth Planet. Sci. Lett.*,
1574 473, 141–153.

1575

1576 Verdel, C., Wernicke, B.P., Hassanzadeh, J., & Guest, B. (2011). A Paleogene extensional arc
1577 flare-up in Iran. *Tectonics*, 30, TC3008.

1578

1579 Vincent, P. (2004). Present-day crustal deformation and plate kinematics in the Middle East
1580 constrained by GPS measurements in Iran and north ern Oman, *Geophys. J. Int.*, 157, 381–398.

1581

1582 Vincent, S.J., Morton, A.C., Carter, A., Gibbs, S., & Barabadze, T.G. (2007). Oligocene uplift of
1583 the western Greater Caucasus: An effect of initial Arabia– Eurasia collision. *Terra Nova*, 19,
1584 160–166.

1585

1586 Whippe, K.X., & Meade, B.J. (2004). Controls on the strength of coupling among climate,
1587 erosion, and deformation in two-sided, frictional orogenic wedges at steadystate. *J. Geophys.*
1588 *Res.*, 109, F1.

1589

1590 Willett., S.D. (1999). Orogeny and orography: The effects of erosion on the structure of
1591 mountain belts. *J. Geophys. Res* 104, 28957–28981.

1592

1593 Wilmsen, M., Fursichfranz, F.T., Fursich, T., Seyed-Emami, K., Majidifard, M.R., & Taheri, J.
1594 (2009). The Cimmerian Orogeny in northern Iran: Tectono-stratigraphic evidence from the
1595 foreland. *Terra nova*, 21, 211-218.

1596

1597 Yassaghi, A., & Madanipour, S. (2008). Influence of a transverse basement fault on along strike
1598 variations in the geometry of an inverted normal fault: Case study of the Mosha Fault, Central
1599 Alborz Range, Iran. *J. Struct. Geol* 30, 1507–1519.

1600

1601 Zanchi, A., Zanchetta, S., Berra, F., Mattei, M., Garzanti, E., Molyneux, S., Nawab, A., &
1602 Sabouri, J. (2009). the Eo-Cimmerian (Late? Triassic) orogeny in North Iran. *Geological*
1603 *Society, London, Special Publication*, 312, 31-55.

1604